European Commission

JRC TECHNICAL REPORT

Impacts of changing weather patterns due to the global warming on black carbon transport and deposition to the Arctic

Dobricic, S.
Pozzoli, L.
Vignati, E.
Russo, S.

2020

Joint Research Centre

EUR 27711 EN

Contact information
Name: Srdan DOBRICIC
Address: European Commission, Joint Research Centre, Directorate C Energy, Transport and Climate, Air and Climate Unit, via E. Fermi 2749, 21027 Ispra -Italy
Email: srdan.dobricic@ec.europa.eu
Tel.: +39 0332 786376

EU Science Hub
https://ec.europa.eu/jrc

JRC99865

EUR 27711 EN

PDF ISBN 978-92-79-54639-6 ISSN 1831-9424 doi:10.2788/879160

Luxembourg: Publications Office of the European Union, 2020

How to cite this report: Dobricic, S., Pozzoli, L., Vignati, E., and Russo, S., Impacts of changing weather patterns due to the global warming on black carbon transport and deposition to the Arctic, EUR 27711 EN , Publications Office of the European Union, Luxembourg, 2020, ISBN 978-92-79-54639-6, doi:10.2788/879160, JRC99865.

Contents

Acknowledgements

We would like to thank Enrico Pisoni (JRC) for reviewing the manuscript and providing a number of comments and suggestions that improved the report legibility and the presentation of our findings.

Authors

Dobricic Srdan, Joint Research Centre

Pozzoli Luca, Joint Research Centre

Vignati Elisabetta, Joint Research Centre

Russo Simone, Joint Research Centre

Abstract

By modifying the albedo of the sea ice, black carbon (BC) deposited during the winter in the Arctic might contribute to the observed reduction of the sea ice cover in the recent years. This study attempts to estimate how the modification of large scale weather patterns due to the climate change impacts the transport of BC to the Arctic and its deposition on the sea ice. A new statistical algorithm has been developed to combine reanalysis estimates of three atmospheric patterns that govern the near-surface warming of the Northern Hemisphere in the winter with model estimates of transport and deposition of BC over the arctic sea ice. It was found that two atmospheric patterns have an impact on high latitudes and are closely linked to the sea ice melting tendency, while the third is limited to the lower latitudes. The combined impact of the three independent atmospheric patterns on winter deposition trends of BC between 1980 and 2015 indicates a decreasing tendency over the first year sea ice cover in the eastern Arctic that melts each summer. On the other hand, the deposition over the multiyear sea ice cover in the central and western Arctic increases. During the last decades the increased BC deposition in the winter could eventually contribute to the enhanced melting of the multiyear sea ice.

1 Introduction

1.1 Ocean-Atmosphere-Sea Ice feedbacks in the Arctic climate system

The Arctic has warmed during the recent decades more strongly than other regions due to the polar amplification of the global warming signal. This results from a combination of global changes and regional feedbacks. First of all the sea ice-albedo feedback, starting in spring when the ice starts to melt and exposing larger fraction of the ocean surface, which absorbs light more effectively. The excess heat accumulated by the ocean delays the start date of freezing, causing thinner winter ice and therefore possible impacts also on the following summer's sea ice cover. In addition to the sea ice-albedo feedback, a combination of other processes contribute to the Arctic amplification, such as cloud and water vapor feedback, temperature feedback, atmospheric and ocean circulation feedbacks (Doscher et al. 2014). The rate of change of the Arctic climate system has been so fast in the last decades, that the expressions "new Arctic" started to be used in the last years. Satellite observation of sea ice cover and concentration, available since the late 1970s, show a decline in summer sea ice extent, with an acceleration in the last decade. Record summer minima occurred in 2002, 2005, 2007 and 2012 (Figure 1-1). The "new Arctic" is also characterized by increased fraction of first year ice (Comiso et al., 2008; Kwok et al., 2009; Maslanik et al., 2011), thinner ice (Rothrock et al., 2008; Kwok and Rothrock, 2009) and increased drift speed (Gascard et al., 2008; Hakkinen et al., 2008; Screen et al., 2011).

Figure 1. Relative sea ice cover in September 2012 when it occupied the minimum area since the start of satellite observations.

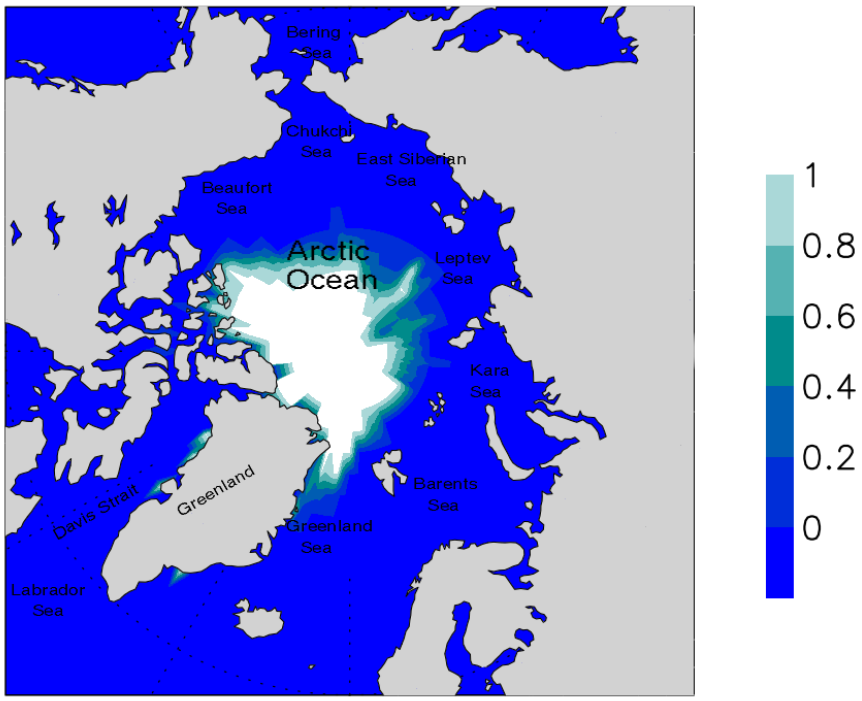

Source: European Commission, JRC, 2016

During winter the decreasing sea ice cover and concentration is mainly occurring in the Barents Sea. A decreasing trend in winter months December-January-February (DJF) sea ice concentrations for the period 1979-2014, up to 20% for decade, was observed over the Barents Sea (National Snow & Ice Data Center, http://nsidc.org/). The Barents Sea is positioned north-east of the Scandinavia (see Figure 1) and is strongly influenced by the warm Atlantic water inflow variability and by atmospheric disturbances originating from mid latitudes (Smedsrud et al. 2013). In particular Smedsrud et al. (2013) hypothesized two positive feedback loops for the Barents Sea. Higher near-surface water temperature in the Barents Sea can be a consequence of larger volume transport from the Atlantic Ocean or of stronger atmospheric heating. Several studies investigated how the varying sea ice cover over the Barents Sea may further produce hemispheric scale impacts in the atmosphere (e.g., Deser et al., 2007; Petoukov et al., 2010; Overland et al., 2010; Screen

et al., 2013; Mori et al., 2014; Cohen et al., 2014; Semenov and Latif, 2015). Mori et al. (2014) for example concluded that sea ice decline in the Barents Sea leaded to more frequent Eurasian blocking situations, which in turn favored cold-air advection to Eurasia and hence severe winters. Cohen et al. (2014) highlighted three potential dynamical pathways linking Arctic amplification to mid-latitude weather: changes in storm tracks, the jet stream, and the planetary waves and their associated energy propagation. Changes in the large scale atmospheric circulation in the North Hemisphere in turn may impact also the transport of atmospheric pollutants, such as black carbon-containing aerosols from the mid-latitudes to the Arctic.

1.2 Effects of Black Carbon on the Arctic climate system

Black carbon (BC) is one of the key components in the Arctic climate system as it affects the Earth radiative balance through several mechanisms (see for example, AMAP 2011, 2015). BC particles directly absorb solar radiation, and above a surface with high albedo, such as snow and sea ice, they warm the atmosphere inside the haze layer and at higher altitudes. On the other hand, the BC may cool the Arctic climate due to surface dimming and decreased poleward heat flux caused by weakened latitudinal temperature gradient from BC heating of the upper troposphere (Shindell and Faluvegi, 2009). Similar results were also confirmed by Sand et al. (2013a,b), while Flanner et al. (2013) found that the temperature response to Arctic BC is highly sensitive to its vertical distribution, BC above 400 hPa cools the Arctic surface, but BC in the lower troposphere and boundary layer determines a strong warming at surface. Aerosols also interact with radiation balance indirectly, by modifying the cloud properties, such as cloud droplet number and size, cloud lifetime and albedo. An additional radiative forcing process is the deposition of BC on snow and ice, which can induce snow and ice melt by warming from radiation absorption. Hadley and Kirchstetter (2012) measured in laboratory how BC snow contamination can reduce snow albedo, with amplified BC radiative perturbation in larger snow grains size, which is also consistent with the parameterizations of BC and soot concentrations in snow included in climate models (Flanner and Zender, 2006; Yasunari et al., 2011; Aoki et al., 2011). Flanner et al. (2013) estimated a sensitivity of about 1.4°C per W/m2 of the Arctic climate to the forcing of BC in snow and sea ice. Sand et al. (2013b) highlighted the importance of BC emissions within the Arctic which deposit to snow and sea ice at a much higher fraction than mid-latitude emissions, thus inducing a greater warming.

1.3 Black Carbon transport and deposition to the Artcic

The studies of BC in the Arctic are further complicated by large uncertainties in space and time of anthropogenic emissions, large variability of vegetation fire emissions, and large variations in atmospheric transport of BC at high latitudes. For example, the AMAP assessment 2015 (AMAP 2015) summarizes the main processes involved in the transport of pollution to high latitudes as described in Stohl (2006). Three main pathways were identified: low-level transport followed by ascent in the Arctic; low-level transport alone; uplift outside the Arctic, followed by slow descent in the Arctic. The transport of pollutants from Eurasia mainly occurs in winter and through all three pathways, while pollution from North America and Asia is mainly occurring through the last pathway only (Stohl, 2006). The Arctic front is a barrier which isolates the Arctic lower troposphere from the rest of the atmosphere. Direct low altitude transport of air pollution from mid-latitudes can occur only when the source region have the same low potential temperatures of the Arctic haze layers, which leaves only North Eurasia as the main source region. The transport pathways are also varying seasonally, with the Arctic front reaching southern latitudes in winter, in particular over Eurasia, facilitating the low altitude transport of pollutants directly from source regions. In summer the Arctic front is generally restricted over high latitudes, the transport mainly occurs by uplift of polluted air and slow mixing and descent into the polar dome. This seasonality in the transport pathways is also reflected in the measured BC concentrations, with winter/spring BC concentrations of 50 ng/m3, and only 3 ng/m3 in summer (see for example mean concentrations for the years 2008-2009 at Alert, Barrow and Zeppelin, Table 2 of Eckhardt et al., 2015).

The seasonal cycle of BC surface deposition in the Arctic is opposite, with larger deposition fluxes in summer due to the more precipitation. A number of studies showed how the parameterization of dry and wet deposition in global models is a key factor in improving the simulation of BC transport to the Arctic (Liu et al., 2011; Browse et al., 2012; Bourgeois and Bey, 2011). Jiao et al. (2014) simulated BC-in-snow concentrations from aerosols deposition simulations from 25 models, showing a poor agreement with a comprehensive set of measurements (Doherty et al., 2010), and a large model variability. The BC residence time in the Arctic ranged from 4 to 23 days across the different models, indicating large differences in the model description of aerosol removal processes. Due to lower insolation in the Arctic during winter and early spring, BC exerts a negligible radiative forcing, but particles that deposit to snow and ice surfaces can re-emerge at the surface

when melt commences in the summer (e.g. Conway et al. 1996), indicating that winter transport and deposition of BC also affect Arctic climate.

The BC concentration and deposition vary considerably also on inter-annual time scale, and large scale atmospheric circulation processes can favor or reduce the transport of pollutants from the main source regions (North America and Eurasia) toward the Arctic. Hirdman et al. (2010) analyzed the long-term trends of equivalent BC (EBC) and sulphate measured at three Arctic stations. They concluded that the observed decreasing trends are mainly driven by changes in the emissions, while the impact of atmospheric circulation can only explain a minor fraction of the downward trend. They found significant correlations between the north Atlantic Oscillation Index (NAOI) and air masses from North America and North Eurasia at both Alert and Barrow, but not for the station at Zeppelin. However, the full understanding of how the transport changes related to the NAOI impact the BC concentrations has not been established

1.4 Objectives

In this study first we use a novel statistical methodology, the Independent Component Analysis (ICA), to connect the sea ice melting trend in the Arctic, observed in winter in the Barents Sea, to the minimum set of independent large scale circulation patterns, which can also approximate the spatial variability of near surface winter temperature trends. We further investigate the relationships between the independent atmospheric patterns and the large scale pollution using a Bayesian approach to estimate the most likelihood BC distribution associated to each atmospheric pattern. We tested this methodology with two independent atmospheric reanalysis products, a reanalysis from the National Center for Environmental Prediction (NCEP, Kalnay et al., 1996), and the ERA-Interim reanalysis (Dee et al., 2008) from the European Centre for Medium-Range Weather Forecasts (ECMWF). The distributions of BC surface concentration, total column and deposition fluxes were taken from a hindcast simulation of tropospheric chemistry composition for the period 1980-2005 with the aerosol-chemistry-climate coupled model, ECHAM5-HAMMOZ (Pozzoli et al., 2011). Two separate simulations were analyzed, one with changing anthropogenic emissions for the entire period, and a second with fixed anthropogenic emissions of the year 2000. With this methodology we are able to quantify the trends and inter-annual variability of BC surface concentrations, load and deposition over winter sea ice in the Arctic associated with large atmospheric circulation induced by present time climate change.

The scope of the study is to apply the new statistical method in order to estimate how winter atmospheric patterns related to the near-surface warming in the winter modify the characteristics of the transport of BC to the Arctic and its deposition on the sea ice. Sections 2 and 3 present the development of the statistical method and data sets used for the estimation. The partitioning of atmospheric transport processes and the related patterns of the pollution and the BC deposition are shown in Section 4, while Section 5 provides the discussion of results and the conclusions.

2 Method

Here we describe a novel method to optimally estimate the relationship between the physical atmospheric state and the large scale pollution. In particular the scope of the method is to find distributions and trends of pollutant concentrations and depositions corresponding to specific atmospheric patterns. By using the Bayesian approach the most likelihood distribution will be found for each pattern. The first subsection will describe the estimation of atmospheric patterns. The second will present the Bayesian estimation method for computing pollution distributions. The third will give an insight on the calculation of linear trends and the fourth will discuss the estimation of uncertainties.

2.1 Independent Component Analysis

2.1.1 Theoretical background

As most planetary scale processes in the atmosphere do not follow normal probability distributions, Hannachi et al. (2009) proposed to apply ICA instead of the commonly used Empirical Orthogonal Functions (EOFs) in climate studies. Here the Fastica algorithm for the ICA method (Hyvärinen et al. 2001) was applied to extract components sharing the minimum information without the gaussianity assumption.

Starting from matrix **X** with rows containing temporal anomalies in the physical space the ICA algorithm finds a linear mapping between a reduced order subspace and anomalies in the physical space in the form:

$$\mathbf{X} \cong \mathbf{AS}. \qquad \text{(Eq-1)}$$

Rows of orthogonal matrix **S**, contain temporally varying independent components, while columns of matrix **A** represent spatially varying intensities. Hereafter columns of matrix A will be named atmospheric patterns.

Although, by requiring the statistical independence of components and avoiding the assumption on the gaussianity, ICA appears to be more general than the EOF method, it has not been applied frequently in climate studies. Hannachi at al. (2011) note that ICA is closely related to Rotated EOFs (REOFs) and estimate independent components with the algorithm based on squared fourth-order statistics.

After performing the partial decomposition on EOFs represented by matrix **V**, REOF rotates them by orthogonal matrix **R** in a way that

$$\mathbf{B} = \mathbf{VR} \qquad \text{(Eq-2)}$$

optimizes a specific predefined criterion $f(\mathbf{B})$. Usually the criterion is some kind of simplicity imposed on the REOFs. Each EOF in **V** can be weighted by different coefficients before the rotation.

On the other hand, it can be shown that independent components **S** may be decomposed by:

$$\mathbf{S} = \mathbf{YR} \qquad \text{(Eq-3)}$$

where $\mathbf{Y} = \mathbf{XU}\boldsymbol{\Lambda}^{-1}$ and Λ is diagonal containing singular values corresponding to EOFs. Even if instead of EOFs **Y** contains principal components, equations (A2) and (A3) have the same form involving a rotation matrix **R**. The ICA estimate, therefore, may be obtained by rotating principal components in a way to produce **S** with maximized independency between components instead of applying the simplicity criterion.

Hannachi et al. (2011) further propose to use the algorithm by Jennrich and Trendafilov (2005) to perform ICA. This algorithm finds **R** as a rotation that minimizes off-diagonal contributions to the Frobenius norm of the covariance matrix resulting from the matrix with elementwise squares formed by all possible orthogonal rotations of **Y**. The algorithm is particularly interesting as it directly links ICA with REOF that is a common method in climate studies.

This study applies the Fastica algorithm by Hyvärinen and Oja, (2000). In Fastica independent components are selected in a way that they also maximize the approximation of the negentropy of the random variable N defined as:

$$N = H\left(y_{gauss}\right) - H\left(y\right), \qquad \text{(Eq-4)}$$

where y_{gauss} is a random variable with the gaussian distribution and the same variance as y and H is entropy. It is demonstrated by the central limit theorem that negentropy is always positive, because the Gaussian variable has the largest entropy of all random variables with the same variance. A simple approximation of the negentropy is:

$$N \propto \left[E\{G(y)\} - E\{G(v)\}\right]^2, \qquad \text{(Eq-5)}$$

where v is a random variable with the gaussian distribution and the unit variance, $E\{\ \}$ the expectation and G is an arbitrary selected nonquadratic function such that its expectation produces a robust approximation of the negentropy (Hyvärinen and Oja 2000). Fastica estimates **S** by iteratively minimizing the gradient of the cost function defined in equation (Eq-5) (Hyvärinen and Oja 2000, Hyvärinen et al. 2001). At the maximum of the negentropy random variables will have the most nongaussian distributions that, as demonstrated by the central limit theorem, correspond to the most independent components (Hyvärinen et al. 2001).

The ICA method assumes the absence of the noise in equation (Eq-1). This may impact the application of ICA in the atmosphere due to the presence of anomalies that are not directly related to the slow temporal change and may mix with estimates of independent components. Here the impact of high frequency signals is reduced by studying anomalies of monthly averages. Furthermore, the noise is alleviated by performing ICA on a reduced subspace defined by several leading principal components. The number of principal components is chosen arbitrary as a tradeoff between supressing the noise and resolving as much as possible sources of observed warming patterns.

2.1.2 Application to atmospheric parameters

In order to perform multivariate analysis of several atmospheric parameters temperature, geopotential height and wind velocity are first transformed into energies. At each horizontal point and pressure level kinetic, potential and internal energies per unit mass are defined as $E_K = |\mathbf{v}|^2/2$, $E_P = gz$ and $E_I = c_V T$ respectively. Here $|\mathbf{v}|$ is the intensity of wind, *z* height of isobaric surfaces and T temperature, whilst g is the acceleration due to gravity and c_V the heat capacity of air at constant volume.

State vectors are formed consisting of kinetic, potential and internal energies at all levels. The statistical processing of energy components is justified by the fact that it processes multivariate state vectors without arbitrary scaling, whilst anomalies of geopotential height and temperature at different levels may be always recalculated after the division by known constants from $\delta z = \delta E_P / g$ and $\delta T = \delta E_I / c_V$. Although wind intensity cannot be easily recovered due to the quadratic form of the relationship, kinetic energy anomalies still may indicate areas with the largest change of wind intensity.

The chosen nonlinearity in the Fastica algorithm is the hyperbolic tangent. For computational reasons, first the eigenvalue decomposition is made on the correlation matrix originating from anomalies and the solution is restricted to the subspace spanned by a small number of eigenvectors with the largest eigenvalues. Independent components are estimated from the subspace consisting of four principal components that are whitened with their corresponding eigenvalues. After the statistical processing spatial and temporal structures of kinetic, potential and internal energies present in atmospheric patterns were visualized in order to check their physical and dynamical consistency. The same setup of the Fastica algorithm also is used for the ERA-INTERIM analysis except that due to the higher number of resolved scales six principal components were necessary to approximate the spatial distribution of near surface temperature trends similarly to four principal components from the NCEP reanalysis.

2.2 Bayesian estimate of atmospheric pollution distributions

We denote by $\mathbf{a}_{Ak}$ the atmospheric pattern for which we estimate the pollutant concentration. It may be a column of mixing matrix **A**. In this case it may be a global three dimensional atmospheric pattern that may span several time steps. It can also be a reduced part of the column of **A** like the regional three or two dimensional distribution. It can also correspond to only one time step of those spanned by the column of matrix **A**.

By vector $\mathbf{a}_{Ck}$ we define the coupled structure including atmospheric and pollution parts, that is $\mathbf{a}_{Ck} = \left(\mathbf{a}_{Ck}^{A}, \mathbf{a}_{Ck}^{P}\right)$. The atmospheric part $\mathbf{a}_{Ck}^{A}$ may be defined on the same spatial and temporal resolution like $\mathbf{a}_{Ak}$. It may also have a different resolution or the spatial and temporal coverage, but it is necessary that there exists a mapping $H\left(\mathbf{a}_{Ck}\right)$ between at least a part of $\mathbf{a}_{Ck}$ and a part of $\mathbf{a}_{Ak}$.

By using the Bayesian theorem the probability of observing $\mathbf{a}_{Ck}$ given $\mathbf{a}_{Ak}$ may be expressed as:

$$p\left(\mathbf{a}_{Ck} \mid \mathbf{a}_{Ak}\right) \propto p\left(\mathbf{a}_{Ak} \mid \mathbf{a}_{Ck}\right) p\left(\mathbf{a}_{Ck}\right). \qquad \text{(Eq-6)}$$

By assuming gaussian distributions for the probabilities Axx becomes:

$$p\left(\mathbf{a}_{Ck} \mid \mathbf{a}_{Ak}\right) \cong const \times \exp\left\{-\frac{1}{2}\left[\mathbf{a}_{Ak} - H\left(\mathbf{a}_{Ck}\right)\right]^{T} \mathbf{D}^{-1}\left[\mathbf{a}_{Ak} - H\left(\mathbf{a}_{Ck}\right)\right] - \frac{1}{2}\mathbf{a}_{Ck}^{T}\mathbf{C}^{-1}\mathbf{a}_{Ck}\right\}, \qquad \text{(Eq-7)}$$

where **D** is the covariance matrix describing the variability of differences between atmospheric anomalies and coupled anomalies mapped on the atmospheric pattern space, while **C** is the covariance matrix of coupled anomalies.

The maximum likelihood solution of Ax2 is the one with the minimum absolute value of the argument of the exponential function. It corresponds to the minimum of the cost function:

$$J = \frac{1}{2}\left[H\left(\mathbf{a}_{Ck}\right) - \mathbf{a}_{Ak}\right]^{T} \mathbf{D}^{-1}\left[H\left(\mathbf{a}_{Ck}\right) - \mathbf{a}_{Ak}\right] + \frac{1}{2}\mathbf{a}_{Ck}^{T}\mathbf{C}^{-1}\mathbf{a}_{Ck} \qquad \text{(Eq-8)}$$

Assuming that the mapping between $\mathbf{a}_{Ck}$ and $\mathbf{a}_{Ak}$ is linear, that is $H\left(\mathbf{a}_{Ck}\right) = \mathbf{H}\mathbf{a}_{Ck}$, *J* becomes a quadratic cost function. In this case the unknown vector $\mathbf{a}_{Ck}$ may be obtained by finding the zero value of the gradient of *J*. Alternatively here we find the minimum of *J* iteratively by a minimizer. The stability of the convergence of the minimizer may be increased by defining a control subspace:

$$\mathbf{z} = \mathbf{Z}^{+}\mathbf{a}_{Ck} \qquad \text{(Eq-9)}$$

Where the matrix **Z** is a square root of the covariance matrix **C** and the subscript "+" indicates the generalised inverse. The cost function becomes:

$$J = \frac{1}{2}\left[\mathbf{H}\mathbf{Z}\mathbf{z} - \mathbf{a}_{Ak}\right]^{T} \mathbf{D}^{-1}\left[\mathbf{H}\mathbf{Z}\mathbf{z} - \mathbf{a}_{Ak}\right] + \frac{1}{2}\mathbf{z}^{T}\mathbf{z} \qquad \text{(Eq-10)}$$

Once the control variable **z** is found by minimizing *J* the most likelihood coupled anomaly is obtained from:

$$\mathbf{a}_{Ck} = \mathbf{Z}\mathbf{z}. \qquad \text{(Eq-11)}$$

The minimization requires the prior estimation of covariance matrix **D**. It is assumed to be diagonal. Elements along the diagonal are assumed to have the constant variance divided by the area of each grid point. The division ensures that the variance is invariant with respect to the grid point area. In order to further simplify the algorithm $\mathbf{a}_{Ck}^{A}$ and $\mathbf{a}_{Ak}$ are estimated at the same spatial resolution. In this way mapping **H** becomes equal to identity **I**.

Matrix **C** is estimated from a long coupled data set with anomalies $\mathbf{x}_{C}$ containing both atmospheric $\mathbf{x}_{C}^{A}$ and pollution concentrations anomalies $\mathbf{x}_{C}^{P}$. Typically the fields come from a coupled atmosphere-chemistry model simulation. Atmospheric and pollution fields can also be estimated separately, for example by separate atmosphere and pollution concentration analysis. It is only important that $\mathbf{x}_{C}^{A}$ and $\mathbf{x}_{C}^{P}$ correspond to the same set of time steps. The covariance matrix of anomalies $E\left\{\mathbf{x}_{C}\mathbf{x}_{C}^{T}\right\}$ is then approximated by

forming the EOF decomposition of coupled anomalies and by maintaining only several EOFs with major eigenvalues. The mapping **Z** between the control space **z** and the physical space $\mathbf{x}_C$ is defined as:

$$\mathbf{Z} \cong \mathbf{V}\mathbf{\Lambda}^{1/2}, \qquad \text{(Eq-12)}$$

where columns of **V** are EOFs with largest eigenvalues and diagonal elements of $\mathbf{\Lambda}$ are their eigenvalues.

The cost function is minimized using the quasi-Newton L-BFGS minimizer (Byrd et al., 1995). Iterations of the minimizer are stopped when the absolute value of the gradient of the cost function becomes small relative to its initial value.

2.3 Linear trends

The linear slope m_k is computed for each independent component $\mathbf{s}_k$. The spatial distribution of trend associated to each independent component is represented as a column of matrix **T**:

$$\mathbf{T} = \mathbf{A}\mathbf{M}, \qquad \text{(Eq-13)}$$

where **M** is a diagonal matrix with linear slopes m_k on the diagonal. Only columns $\mathbf{t}_k$ corresponding to linear slopes with large statistical significance are selected for the further analysis.

The full reanalysis trend t_{FiA} of a variable at each geographical point *i* is then approximated by the reconstructed trend t_{RiA} that is estimated from approximated anomalies:

$$\tilde{\mathbf{x}}_{iA} = \sum_k a_{kiA}\mathbf{s}_k\Delta_k, \qquad \text{(Eq-14)}$$

where Δ_k equals to one if the trend associated with the *k*-th independent component is statistically significant and to zero otherwise.

The pollution trend is then estimated by:

$$\tilde{\mathbf{x}}_i^P = \sum_k a_{ki}^P\mathbf{s}_k\Delta_k \qquad \text{(Eq-15)}$$

Trends are calculated by the Sen-Kendall method (Sen 1968). The statistical significance for all trends is set to the 0.05 level and is estimated by the Mann-Kendall test (Mann 1945). Areas with significant trends are marked in figures, except for atmospheric patterns that have spatially uniform slopes.

2.4 Estimation of uncertainties

The uncertainties of the trend estimation are addressed by processing several reanalysis and modelling estimates of original data sets. In this report two atmospheric reanalysis will be combined with two simulations of a coupled ocean-atmosphere model in which the emissions were changed spanning time windows of 12 and 25 years. This produces six independent estimates of pollution trends. Their spread will represent an estimate of the uncertainty.

3 Data

3.1 Atmospheric data

The statistical processing of atmospheric data was made over the whole troposphere and the lower stratosphere up to 10 mb in order to detect the eventual coupling between the troposphere and the stratosphere. Two reanalysis data sets were used. The first consisted of monthly averaged wind intensity, geopotential height and temperature from the NCEP reanalysis (Kalnay et al. 1996) available on 17 standard pressure levels from 1000 to 10 mb and the topography with the horizontal resolution of 2.5^0. The uncertainty linked to the particular reanalysis data set is addressed by additionally processing anomalies from ERA-Interim reanalysis (Dee et al. 2008). This reanalysis data set used the atmospheric model with a higher spatial resolution, and the data assimilation scheme applied additional treatment of biases estimated for observations and the atmospheric model. Anomalies are computed at the same horizontal resolution of 2.50, but 38 levels are used between 1000 and 10 mb. Although the statistical processing was made on the same horizontal resolution, anomalies originate from a higher resolution model and may contain a larger number of resolved scales and processes than the NCEP reanalysis.

The estimation of independent patterns was insensitive to the lowering of the top layer down to 100 mb (not shown). This can be explained by the fact that layers are scaled by the square root of the pressure thickness in order to preserve the variance with respect to the layer mass change. As a consequence the lower stratosphere is weighted by an order of magnitude less than the troposphere and its variability does not impact significantly the statistical processing.

Energy anomalies are computed in December, January and February from 1980 till 2015. They are detrended at each point by subtracting monthly means. The whole set contains 36 samples with anomalies of kinetic, potential and internal energies on 17 atmospheric levels and during the three winter months. The horizontal grid is thinned along latitudes to produce points with the same area preserving the variance with respect to horizontal geometry. Values at each level are multiplied by the square root of the pressure thickness to preserve the variance with respect to the change of the layer mass.

Near-surface temperature anomalies in the winter are evaluated by studying anomalies of temperature at isobaric surface of 1000 mb (T1000) that is positioned close to the sea level. In this study also anomalies of geopotential heights in the lower troposphere may be important, because by assuming geostrophy they may indicate mean transport anomalies of the atmospheric pollution from the middle latitudes to the Arctic. To represent these anomalies we will evaluate also the height of the 850 mb isobar surface (H850).

In the 1980-2015 period a dramatic reduction of the sea ice occurred in the Arctic. This is also the so called "satellite era" when T1000 is well observed by in situ and satellite observations when satellite observations of radiances provide accurate monitoring of the temporal and spatial variability of the vertically integrated internal energy, VIIE (Kalnay et al. 1996; Vinnikov et al. 2006). On the other hand, the observational monitoring of the vertical distribution of atmospheric parameters may be less accurate in remote areas (Vinnikov et al. 2006). Thus, the study of trends of meteorological parameters is mainly restricted to T1000 that is close to the surface and assumed to be well observed. In the winter there are very few near-surface observations of temperature over the Arctic sea ice, and there the reanalysis of T1000 may be less accurate. Nevertheless, the sea ice coverage is well observed by satellites on the monthly frequency and we assume that its connection with atmospheric conditions at large scales may be resolved by the reanalysis. Furthermore, over the ocean the sea surface temperature is also continuously observed by satellites at the monthly frequency providing an accurate boundary constraint on the near surface temperature in the reanalysis over ice free areas.

Figure 2 shows the estimate of the T1000 trend averaged over winter months from 1980 to 2015. The major well-known feature is that T1000 trends vary significantly between positive values over the Arctic Ocean, the North Atlantic and the North Pacific, and negative over the Siberia and the Equatorial Pacific. In particular there is a prominent dipole between the strong warming over the Arctic and the strong cooling over the Siberia. Another large dipole is between the cooling in the Eastern and in the Western Pacific Ocean over the tropics. There are also smaller spots with the enhanced warming over the North America, the North Africa and the Asia. The general structure is present in all winter months, while the interseasonal variations are localized on small scales. An exception from this picture is an increasing warming trend over the Eastern Mediterranean and the Middle East in February that was less evident in December and January. All areas with strong warming and cooling tendencies also have statistically significant trends.

Figure 2. T1000 trends from 1980-2015 (10^{-2} K $year^{-1}$) as estimated by a) NCEP and b) ERA-INTERIM reanalysis.

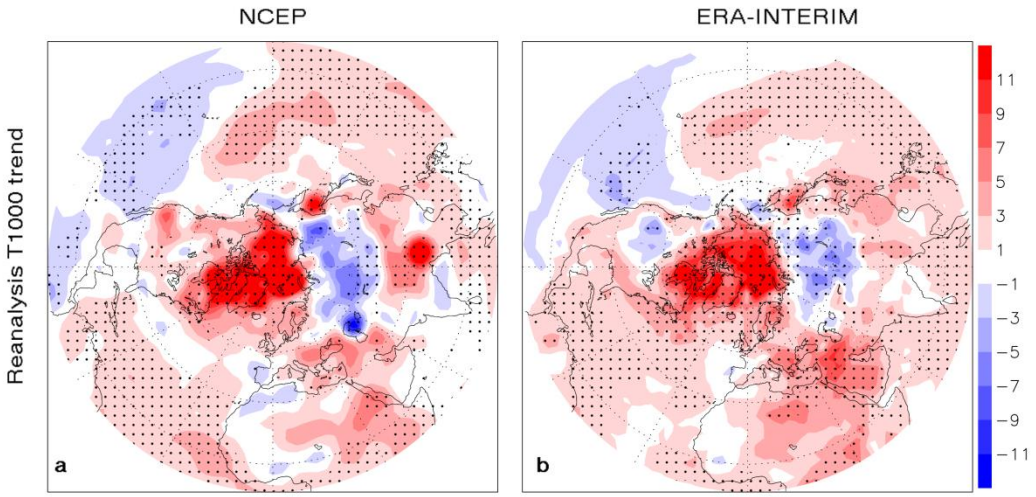

Source: European Commission, JRC, 2016

The winter trend of H850 estimated by the two reanalysis is shown in Figure 3. The circulation trend in the lower troposphere is characterized by anticyclones over the North Pacific and the Arctic Ocean, while there is the cyclonic tendency over Europe, the Indian Ocean and the western part of the tropical Pacific. These dynamical features do not indicate a significant change of the atmospheric transport from the mid latitudes to the Arctic Sea ice.

Figure 3. H850 trends from 1980-2015 (10^{-1} m $year^{-1}$) as estimated by a) NCEP and b) ERA-INTERIM reanalysis.

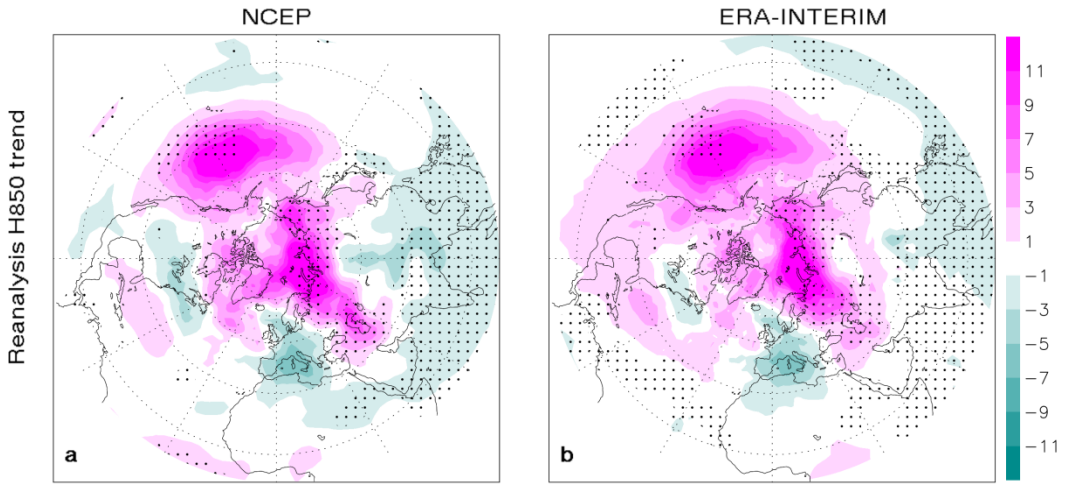

Source: European Commission, JRC, 2016

The statistical processing was insensitive to a small change of the starting and the ending year. The reduction from 36 to the last 10 years significantly changed the results (not shown). This could be expected, because at a short time period independent patterns reflect a different type of the variability and the uncertainty of the statistical processing increases. The choice of 36 samples may result in a much better estimate of the variance while still satisfying the assumption on the linearity of the processes.

3.2 Global simulations of Black Carbon

Simulated concentrations and deposition fluxes of black carbon were obtained from two hindcast simulations of the chemical composition of the troposphere for the period 1980-2005 with a coupled climate-chemistry-aerosol global model, ECHAM5-HAMMOZ (Pozzoli et al., 2011). One simulation was performed with varying anthropogenic emissions, while the second one using anthropogenic emissions constant at level of year 2000.

The simulation of tropospheric chemistry composition for the period 1980-2005 using the ECHAM5-HAMMOZ is described in details by Pozzoli et al. (2011). ECHAM5-HAMMOZ is a fully coupled aerosol-chemistry-climate model, composed of the general circulation model (GCM) ECHAM5, the tropospheric chemistry module MOZ, and the aerosol module HAM. The ECHAM5-HAMMOZ model is described in detail in Pozzoli et al. (2008a). The model has been extensively evaluated in previous studies (Stier et al., 2005; Pozzoli et al., 2008a,b; Auvray et al., 2007; Rast et al., 2014) with comparisons to several measurements and within model inter-comparison studies. The horizontal resolution is ca. 2.8◦ × 2.8◦ degrees, and 31 vertical levels from the surface up to 10 hPa. The simulation was nudged for the entire period to represent the reanalysis meteorological fields from the ECMWF ERA-40 re-analysis (Uppala et al., 2005) until 2000 and from operational analyses (IFS cycle-32r2) for the remaining period (2001–2005). The anthropogenic emissions of CO, NOx, and VOCs for the period 1980–2000 are taken from the RETRO inventory (Schultz et al., 2007; Endresen et al., 2003; Schultz et al., 2008). The AeroCom hindcast aerosol emission inventory (Diehl et al., 2012) was used for the annual total anthropogenic emissions of primary black carbon (BC), organic carbon (OC) aerosols and sulfur dioxide (SO2). Total black carbon emissions remained constant during the simulated period, around 4.9 Tg/year. However, these global numbers mask that the global distribution of the emission largely changed, with reductions over North America (-35%) and Europe (-45%), balanced by strong increases in the economically emerging regions, such as East and South Asia (30% and 70% increase, respectively). Biomass burning, from tropical savannah burning, deforestation fires, and mid-and high latitude forest fires are largely linked to anthropogenic activities but fire severity (and hence emissions) are also controlled by meteorological factors such as temperature, precipitation and wind. The compilation of inter-annual varying biomass burning emissions published by Schultz et al. (2008) was used.

This model simulation is included in the hindcast multi model experiment of the AeroCom project. A number of studies have already analyzed and evaluated this dataset, for example, Pan et al. (2015) looked at the aerosol simulation over South Asia; Tsigaridis et al. (2014) evaluated the simulated organic aerosols globally; Kim et al. (2014) focused on the transport of mineral dust from North Africa; Pausata et al. (2013; 2012) analyzed the impact of the NAO on surface O3 and PM2.5 concentrations over Europe. An extensive evaluation of the ECHAM5-HAMMOZ simulation is available in the above mentioned studies.

In this report we will focus on the black carbon transport patterns from North Hemisphere mid-latitudes towards the Arctic during winter months. Thus we first present an overview of simulated winter (DJF) black carbon fields, such as emissions, surface concentrations, total column load, and deposition, which were used for the statistical analysis. Figure 4 shows the distribution of BC wet deposition, total column mass, surface concentration and emissions averaged over the entire period for winter season (DJF) over the Arctic and the North Hemisphere mid latitudes, where largest emissions are located. The transport and deposition of BC towards the Arctic during winter mainly occur through the lifting of polluted air masses by the Arctic front, associated with cloud formation and precipitation by which BC can be scavenged and deposited. A low level transport can occur when the source regions are sufficiently cold and the Arctic front can be located as south as 40°N, which allows polluted air from northern Eurasia to penetrate the entire Arctic at low altitudes on time scales of 10 to 15 days (Stohl et al., 2006). In general a large gradient between the Arctic and the mid-latitudes can be noted for the considered fields, due to the presence of a “Polar dome” of colder air, which practically isolate the entire Arctic lower troposphere from the rest of the atmosphere.

In the hindcast simulation with varying anthropogenic emissions, the total BC emissions during the simulated period decreased over a large part of the Northern Hemisphere, around 2-30% over Europe, North America and Japan, more than 50% over Russia. On the other hand emissions increased in North West Canada and by more than 30% in Asia. These emission changes determined decreasing trends of BC surface concentrations which extend over the entire Arctic region, with largest reductions over the Barents Sea and Eastern Arctic Ocean. Small increasing trends are simulated over the North Pacific Ocean, the Hudson Bay, Labrador and South of Greenland. A similar pattern is observed for the BC wet deposition with a stronger positive trend over the Arctic Canadian Archipelago and West Greenland. The BC total column load shows smaller trends and positive, below 1%, over almost the entire Arctic, except the Barents, Kara and Leptev Seas (Figure 5).

Figure 4. Multi-annual (1980-2005) winter means (DJF) of BC wet deposition (a), total column load (b), surface concentration (c) and total emissions (d) simulated by the ECHAM5-HAMMOZ model with varying anthropogenic emissions.

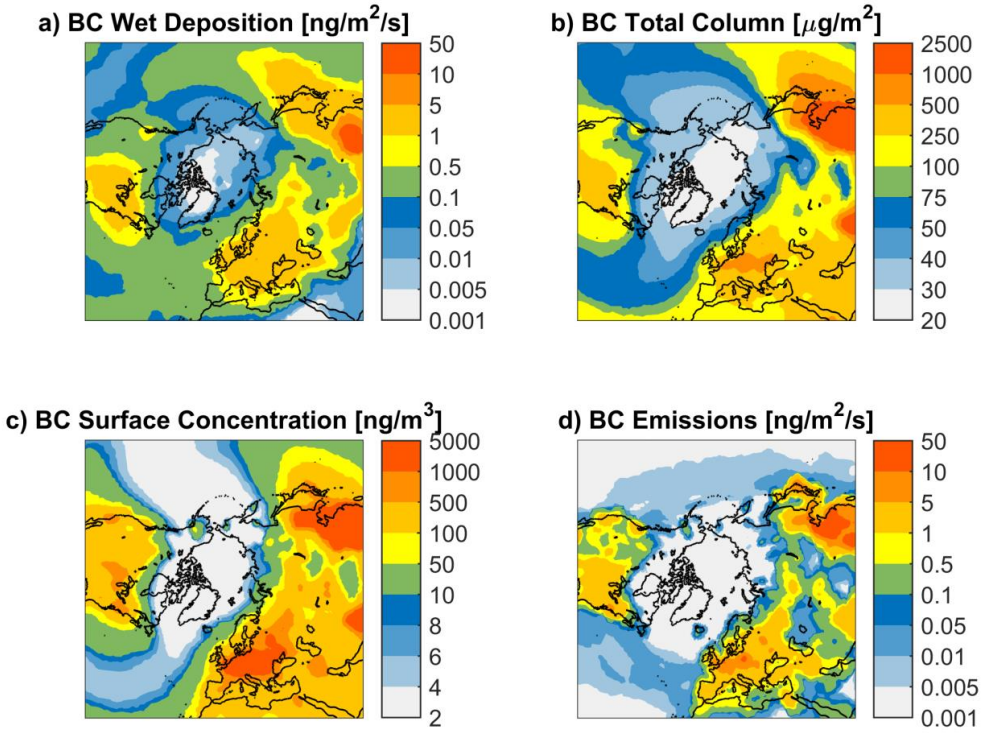

Source: European Commission, JRC, 2016

Figure 5. Changes in winter (DJF) BC wet deposition (a), total column load (b), and surface concentration (c), expressed as percentage per year of the multi-annual winter means (Figure 3-3). The change in total BC winter (DJF) emissions is shown as difference between 5-year averages of the periods 2001-2005 vs 1981-1985.

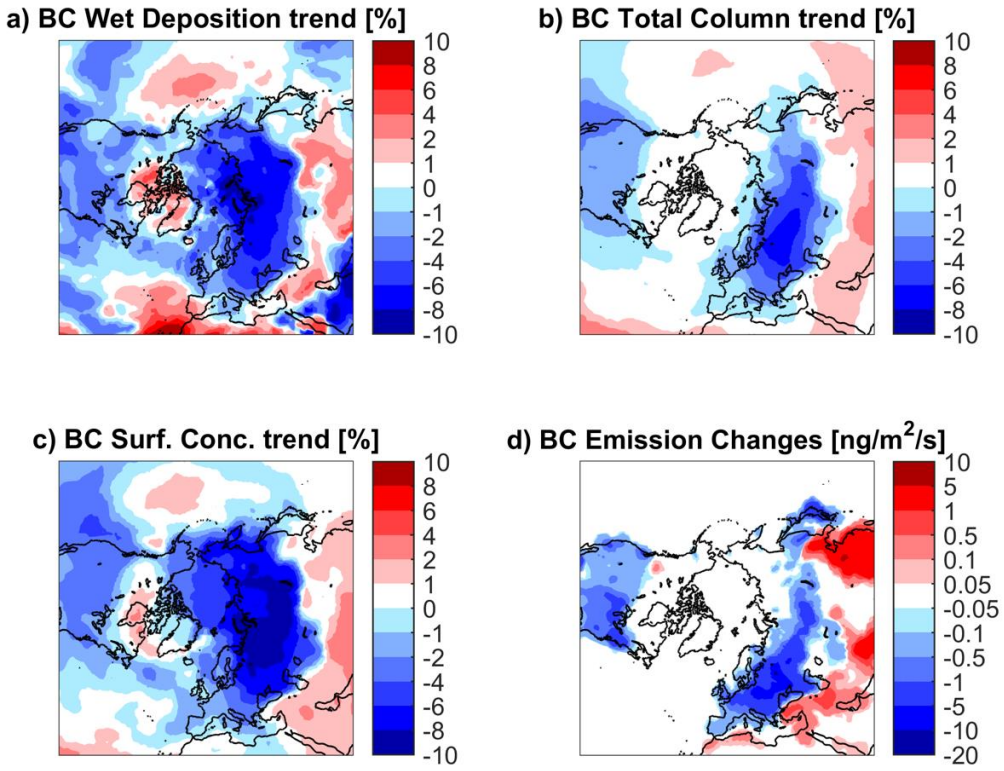

Source: European Commission, JRC, 2016

NCEP and ERA-INTERIM reanalysis from 1980 to 2015 are combined with three sets of coupled atmosphere-chemistry global simulations. This produces six estimates of tendencies for the transport and the deposition of BC to the Arctic described in Section 4. The first two are named NCEP-VA and ERA-VA. They combine the coupled simulation in with realistic temporally variable BC emissions with NCEP and ERA-INTERIM respectively in the period 1993-2005. It was necessary to choose this period, because the sudden drop of emissions from Eastern Europe and Russia in the early nineties introduced a strong change in the transport variability that was impossible to resolve by the statistical method (not shown). The third and the fourth estimates are named NCEP-ST1 and ERA-ST1. They are made for the same time period as NCEP-VA and ERA-VA, but anthropogenic emissions in the coupled global simulation are fixed at the level of the year 2000. The last two estimates named NCEP-ST2 and ERA-ST2 are made with the same simulation as NCEP-ST1 and ERA-ST1, but using the entire simulation from 1980 to 2005. Differences between estimates are summarized in Table 1.

Table 1. The summary of differences between the six estimates

Estimate name	**Atmospheric reanalysis**	**Emissions**	**Period**
NCEP-VA	NCEP	Temporally varying	1993-2005
ERA-VA	ERA	Temporally varying	1993-2005
NCEP-ST1	NCEP	Fixed year 2000	1993-2005
ERA-ST1	ERA	Fixed year 2000	1993-2005
NCEP-ST2	NCEP	Fixed year 2000	1980-2005
ERA-ST2	ERA	Fixed year 2000	1980-2005

Source: European Commission, JRC, 2016

4 Results

4.1 Reconstruction of observed T1000 and H850 trends by the combined action of the three independent components

After performing the ICA decomposition we select independent components with statistically significant trends. Three independent components with significant trends arise from the NCEP reanalysis (Dobricic et al. 2015). They are named according to prevailing large scale patterns described by each independent component: North Atlantic Oscillation (NAO), Scandinavian Blocking (SB) and El-Nino –Southern Oscillation (ENSO). All three patterns are associated with the rise of the hemispheric average of T1000 in the winter. The same set of independent components is detected in the ERA-INTERIM reanalysis (Dobricic et al. 2015). However in ERA-INTERIM only NAO has a statistically significant trend. The trend of SB becomes significant at the 0.1 level, while the trend of ENSO is insignificant. In both NCEP and ERA-INTERIM reanalysis the hemispheric average of the T1000 trend of anomalies reconstructed by the three patterns is positive. It accounts for about one half of the full trend estimated by the reanalyses.

The combination of the three selected independent components approximates the spatial variability of the trend observed by NCEP and ERA-INTERIM reanalysis. By comparing Figures 6 and 2 it can be seen that in the NCEP reanalysis the reconstruction depicts all dominant features of observed trends. It also resolves many small scale features like warming spots over the North America and the Asia. The evolution from December to February is very similar depicting the increase of the warming trend over the Eastern Mediterranean and the Middle East. There are also some small scale differences like opposite weak trends over the Central Europe in January or the slightly stronger cooling over the Equatorial Pacific and the slightly weaker warming over the Equatorial Atlantic. The strong warming in the Arctic is localized to the average position of the edge of the sea ice cover, while in the observed trend it also spreads over the ice covered Arctic Ocean. Another difference is that in the approximated estimate the statistical significance of trends covers a much larger area including many places where the trend is weak. The comparison of figures 4-1 and 3-1 further shows that trends of T1000 reconstructed by the three patterns from the ERA-INTERIM reanalysis also approximate the spatial distribution of reanalysis estimates, although, like for NCEP, the intensity is mostly underestimated.

The reconstruction of H850 trends (Figure 7) depicts the major features of circulation anomalies in the lower troposphere (Figure 3) like the presence of two anticyclones over the North Pacific and the Arctic Ocean and cyclones over Europe, North America and southern Asia. The reconstructed field is significantly smoother than original reanalysis estimates.

Figure 6. Trend of winter T1000 between 1980 and 2015 (10^{-2} K $year^{-1}$) reconstructed by three independent components: a) NCEP and b) ERA-INTERIM. Dots indicate statistically significant trends

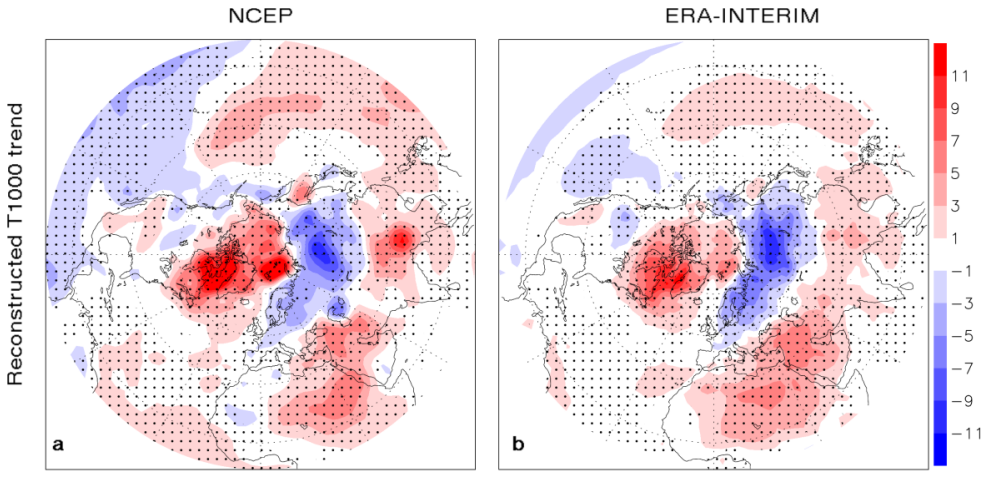

Source: European Commission, JRC, 2016

Figure 7. Trend of winter H850 between 1980 and 2015 (10^{-1} m $year^{-1}$) reconstructed by three independent components: a) NCEP and b) ERA-INTERIM. Dots indicate statistically significant trends.

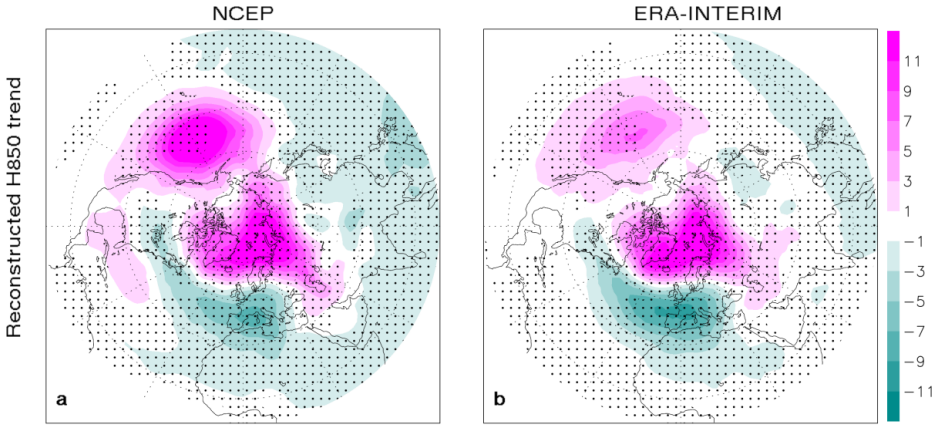

Source: European Commission, JRC, 2016

4.1.1 NAO pattern trends

In the NCEP reanalysis the major structure of T1000 winter trend related to the North Atlantic Oscillation (NAO) pattern is the warming over the North American side of the Arctic with the maximum over the Canadian Archipelago and the cooling over the north part of Siberia that is also associated with a broad and weak warming over the central and southern Asia (Figure 8a). The NAO pattern is initiated in December by the circulation anomaly over Scandinavia closely related to the sea ice cover anomaly over the Barents Sea (Dobricic et al. 2015). The tendency of the formation of the anticyclonic anomaly is related to the tendency of the sea ice cover reduction. The coupling of the anticyclonic tendency near the surface with the pre-existing anticyclonic tendency of the polar stratospheric vortex imitates the formation of the Arctic oscillation (AO) in January and February with the reduction of the intensity of westerlies and the warming over the North American part of the Arctic. The AO structure in January and February dominates the winter trend of the NAO pattern of the H850 field (Figure 8d). There is the anticyclonic anomaly over the Arctic Ocean and the cyclonic anomaly over the North Atlantic. This circulation structure indicates the negative trend of NAO. Very similar patterns of T1000 and H850 (Figure 9a,d) are estimated from the ERA-INTERIM reanalysis. The major difference is that in ERA-INTERIM the trend of the NAO pattern is stronger.

4.1.2 SB pattern trends

The T1000 trend associated with the Scandinavian Blocking (SB) pattern from the NCEP reanalysis is characterized by a strong heating in the area of the major winter sea ice loss in the Barents Sea and the cooling over Siberia (Figure 8b). The H850 trend related to the SB pattern (Figure 9e) shows the anticyclonic tendency over the northern part of Siberia that is dynamically consistent with the cooling over Siberia and warming over the Arctic Ocean, because it advects the warm air from the south to the Barents Sea and the cold air from the arctic to Siberia. It was found by Dobricic e al. (2015) that the tendency of this pattern over the Arctic is strongly coupled with negative temperature tendency over the Tropical Pacific (Figure 9b). In January and February the planetary wave, initiated in December by the negative temperature anomaly over the Tropical Pacific, is amplified over the northern part of Siberia and propagates back towards the Tropical Pacific. It is trapped in the troposphere, because the negative anomaly over the Pacific imposes the stratospheric vortex anomaly of the opposite sign than the tropospheric anomaly in the Arctic. The same pattern is estimated from the ERA-INERIM reanalysis and has a similar intensity of the tendency. However, in ERA-INTERIM this pattern becomes statistically significant only at the 0.1 level (Dobricic et al. 2015).

4.1.3 ENSO pattern trends

The El Nino – Southern Oscillation (ENSO) pattern represented in the NCEP reanalysis shows a cooling trend over the Tropical Pacific, but it does not show a significant imprint in the Arctic region (Figure 8c,f). In the ERA-INTERIM reanalysis the ENSO pattern averaged over the winter is hardly detectable (Figure 9c,f). The ENSO pattern has a weak trend in the NCEP reanalysis, but its tendency is statistically insignificant in the ERA-

INERIM reanalysis (Dobricic et al. 2015). Therefore, we may assume that it is less important for estimating trends of the atmospheric transport of black carbon from the middle latitudes to the Arctic.

Figure 8. T1000 (10^{-2} K $year^{-1}$) and H850 (10^{-1} m $year^{-1}$) trends between 1980 and 2015 of atmospheric patterns estimated from the NCEP reanalysis: a) and d) NAO, b) and e) SB, c) and f) ENSO.

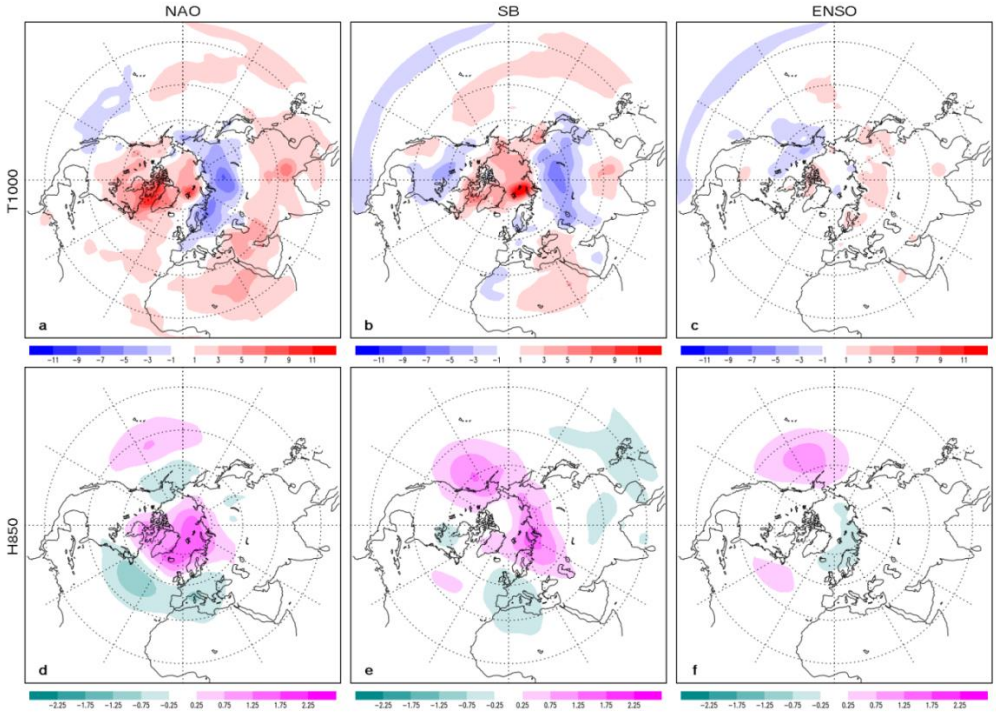

Source: European Commission, JRC, 2016

Figure 9. T1000 (10^{-2} K $year^{-1}$) and H850 (10^{-1} m $year^{-1}$) trends between 1908 and 2015 of atmospheric patterns estimated from the ERA-INTERIM reanalysis: a) and d) NAO, b) and e) SB, c) and f) ENSO.

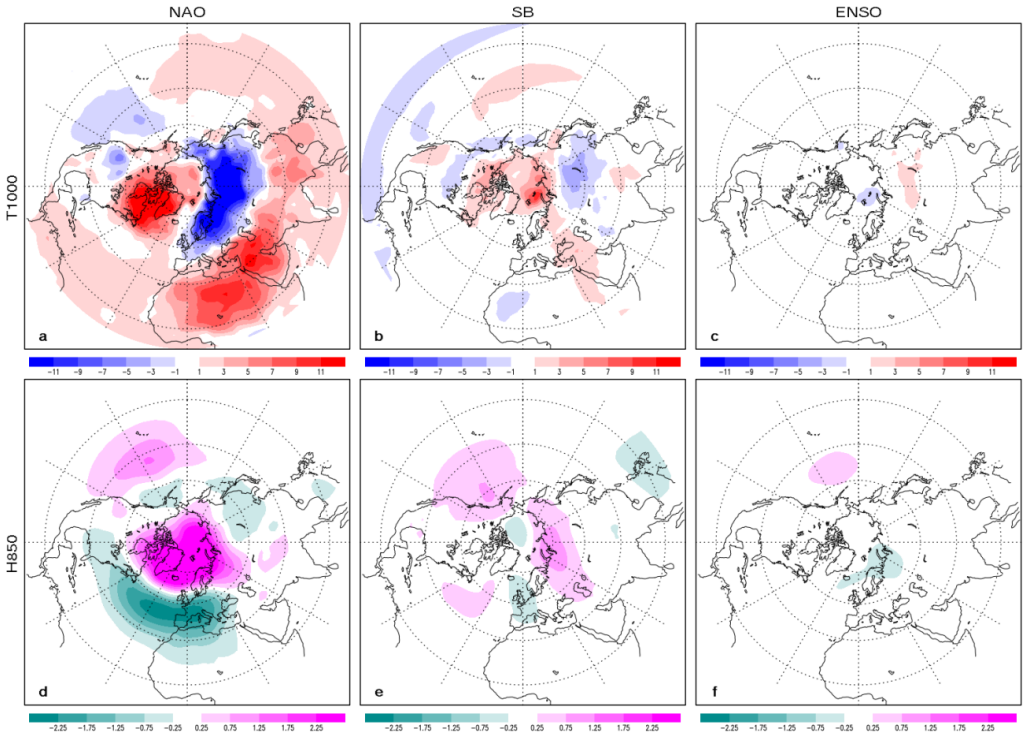

Source: European Commission, JRC, 2016

4.2 Black Carbon deposition and load trends reconstructed by the three components

The trend of the wet deposition reconstructed from the three atmospheric components is shown in Figure 10. Estimates made by 6 combinations of atmospheric reanalyses and chemistry models (see Section 3.2 and Table 1 for the description) shows both areas with positive and negative tendencies in the BC wet deposition. Clearly the atmospheric transport changes due to the global warming impact diversely different areas of the Arctic sea ice.

Figure 10. Trends of BC deposition ($5*10^{-6}$ ng/m^2/s) estimated by: a) NCEP-VA, b) ERA-VA, c) NCEP-ST1, d) ERA-ST1, e) NCEP-ST2 and f) ERA-ST2. Dots indicate statistically significant trends.

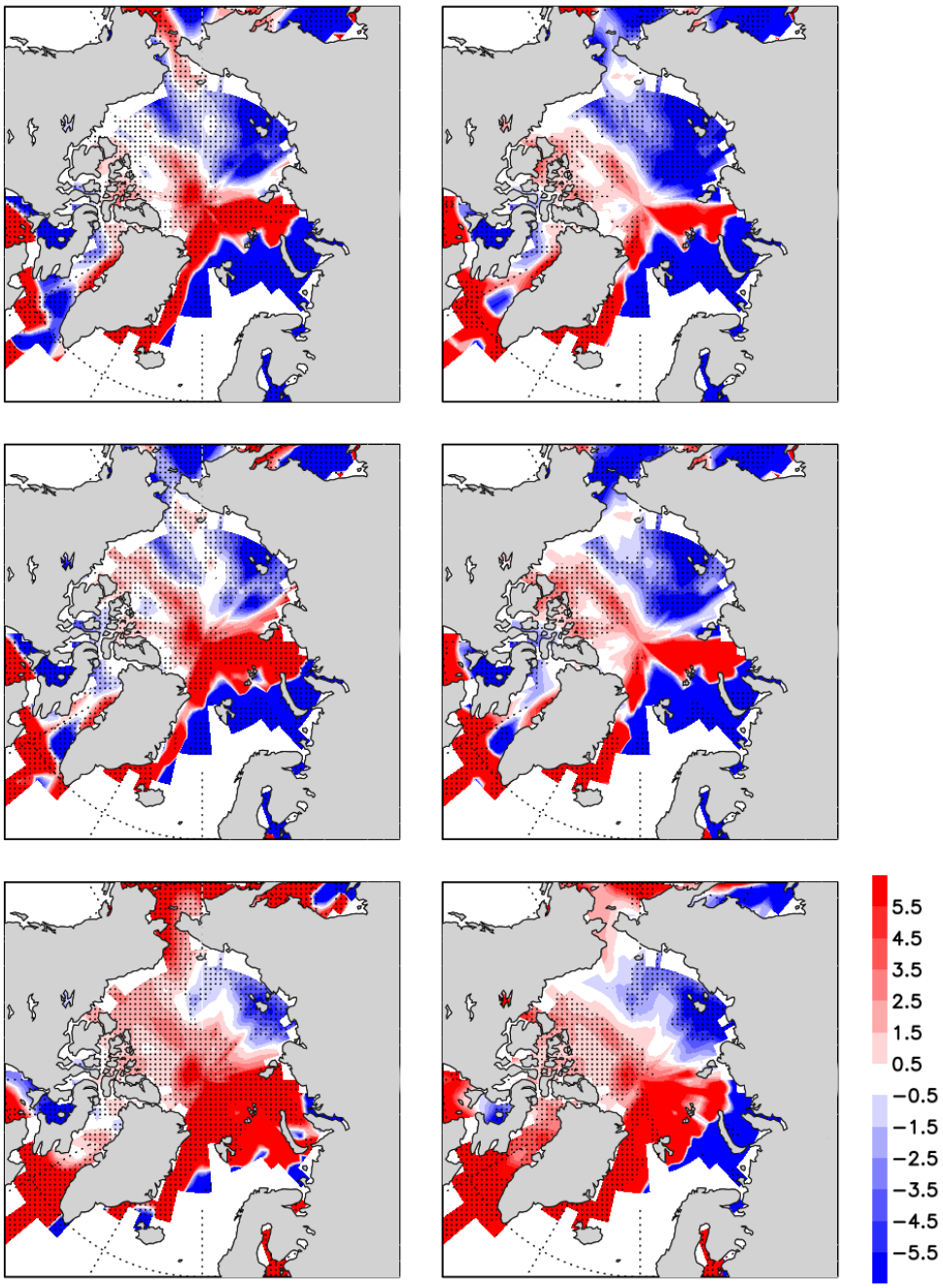

Source: European Commission, JRC, 2016

All six estimates indicate statistically significant negative deposition tendencies in the Laptev, East Siberian and Chukchi Seas. In the Barents Sea there is a slight disagreement between the estimates, but most of them indicate the reduction of the deposition.

On the other hand all six estimates indicate an increase of the deposition north of the Canadian Archipelago, Greenland, Svalbard and the Kara Sea. The positive tendency is especially strong in NCEP-ST2 and ERA-ST2 estimates that used the longest data set for the estimate of coupled EOFs. The positive tendency extends over the central part of the Arctic Ocean. Most of the estimates also indicate an increase of the deposition over the Davis Strait and the Labrador Sea.

The atmospheric load of BC reconstructed by the three components is shown in Figure 11. In all estimates it shows a net increasing trend over the Arctic and the decreasing trend over the mid latitudes. The winter H850 trend shown in Figure 7 indicates that the increase of the load of BC over the Arctic is related to the presence of the anticyclonic circulation trend. Dynamically it imposes stable conditions in which the pollution may accumulate in the atmosphere. The H850 trend is estimated differently by each estimate (Figure 12), but there is the agreement on the estimate of major features like the anticyclonic trend over the Arctic and the North Pacific and the cyclonic trend over Northern Europe and the eastern part of Siberia.

Figure 11. Trends of BC load (10^{-5} mg/m^2/year) estimated by: NCEP-VA (top left), ERA-VA (top right), NCEP-ST1 (centre left), ERA-ST1 (centre right), NCEP-ST2 (bottom left) and ERA-ST2 (bottom right). Dots indicate statistically significant trends.

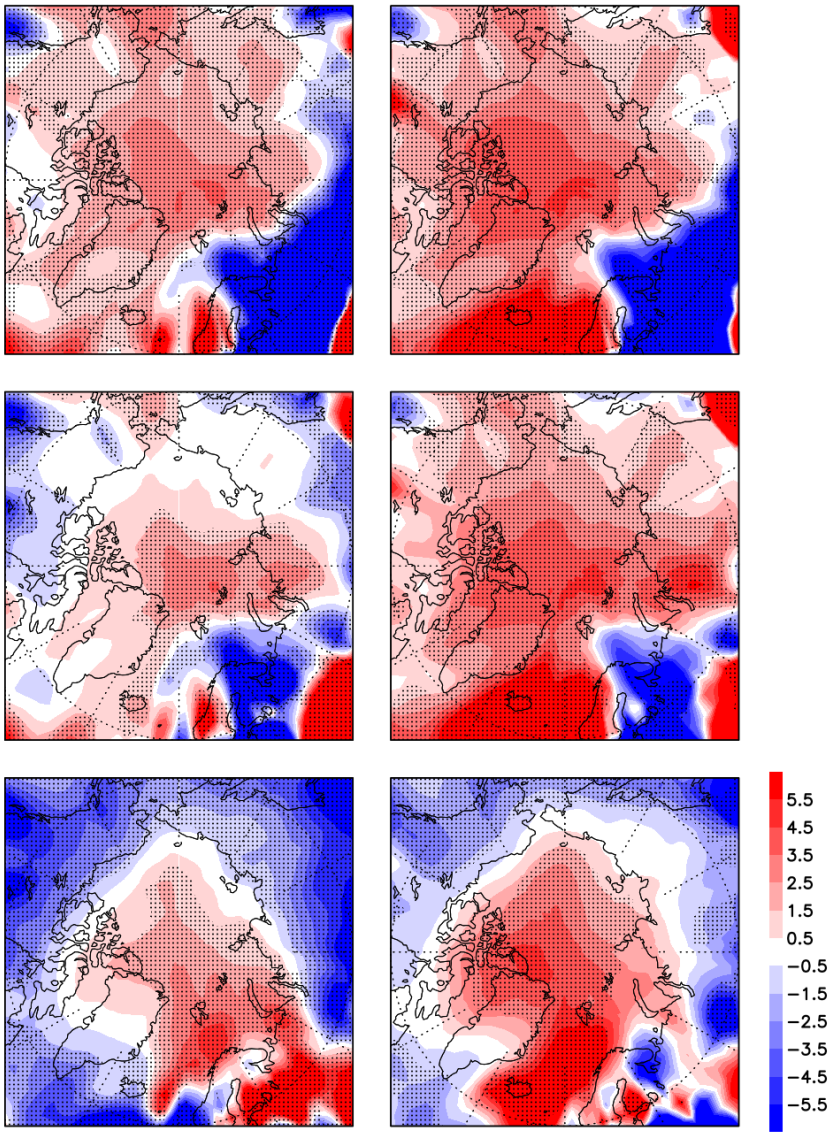

Source: European Commission, JRC, 2016

Figure 12. Trends of H850 (10^{-1} m $year^{-1}$) estimated by: NCEP-VA (top left), ERA-VA (top right), NCEP-ST1 (centre left), ERA-ST1 (centre right), NCEP-ST2 (bottom left) and ERA-ST2 (bottom right). Dots indicate statistically significant trends.

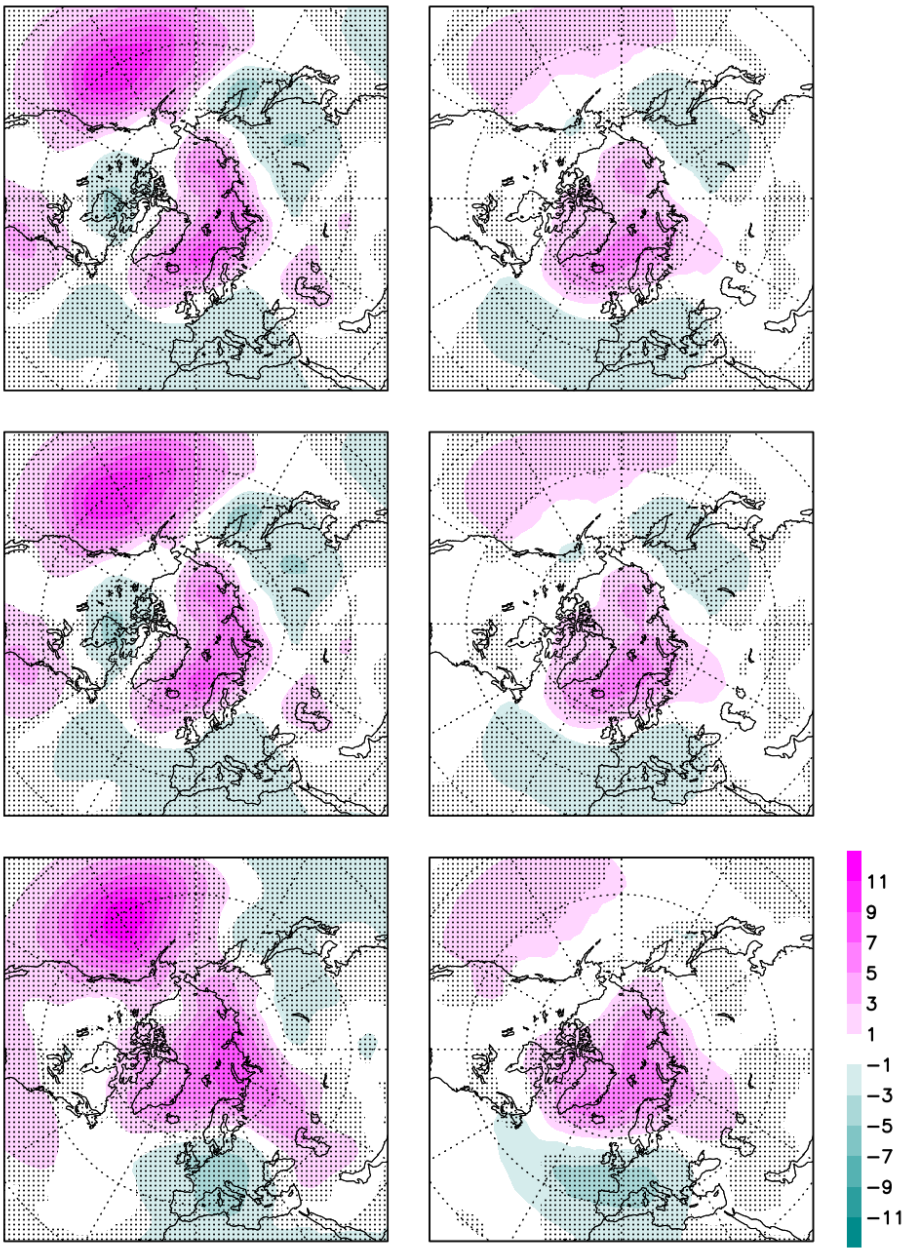

Source: European Commission, JRC, 2016

4.2.1 Black Carbon deposition and load trends related to NAO

The BC deposition trend related to NAO (Figure 13) show the strong decreasing trend north of the Euro-Asian coast and mostly the absence of the trend north of America and Greenland. The load (Figure 14) has the positive trend over the most of the Arctic. The difference between the deposition and load trends is especially evident in February, shown in Figures 15 and 16, when the NAO index by the NAO pattern is the most pronounced (Dobricic et al. 2015). In February the NAO related deposition is characterized by the negative trend over the most of the Arctic, while the load has a positive trend. Clearly, the anticyclonic trend imposes the reduction of the precipitation and BC remains suspended in the atmosphere. The impact of the increased BC concentration in the atmosphere on surface temperatures in the Arctic depends on the altitude of the aerosol layer (AMAP, 2015). A separate estimation of the relationship between the BC concentration trend at each model level in ECHAM5-HAMMOZ and the NAO pattern trend is made by the same methodology to estimate deposition and load trends. It can be seen in Figure 17 that the maximum increasing trend of the

atmospheric concentration of BC is positioned high in the troposphere at the height of about 9-10 km. According to (AMAP, 2015) in this case it may have a small effect on the trend of near-surface temperatures.

Figure 13. Trends of BC deposition related to NAO ($5*10^{-6}$ ng/m^2/s) as estimated by: NCEP-VA (top left), ERA-VA (top right), NCEP-ST1 (centre left), ERA-ST1 (centre right), NCEP-ST2 (bottom left) and ERA-ST2 (bottom right).

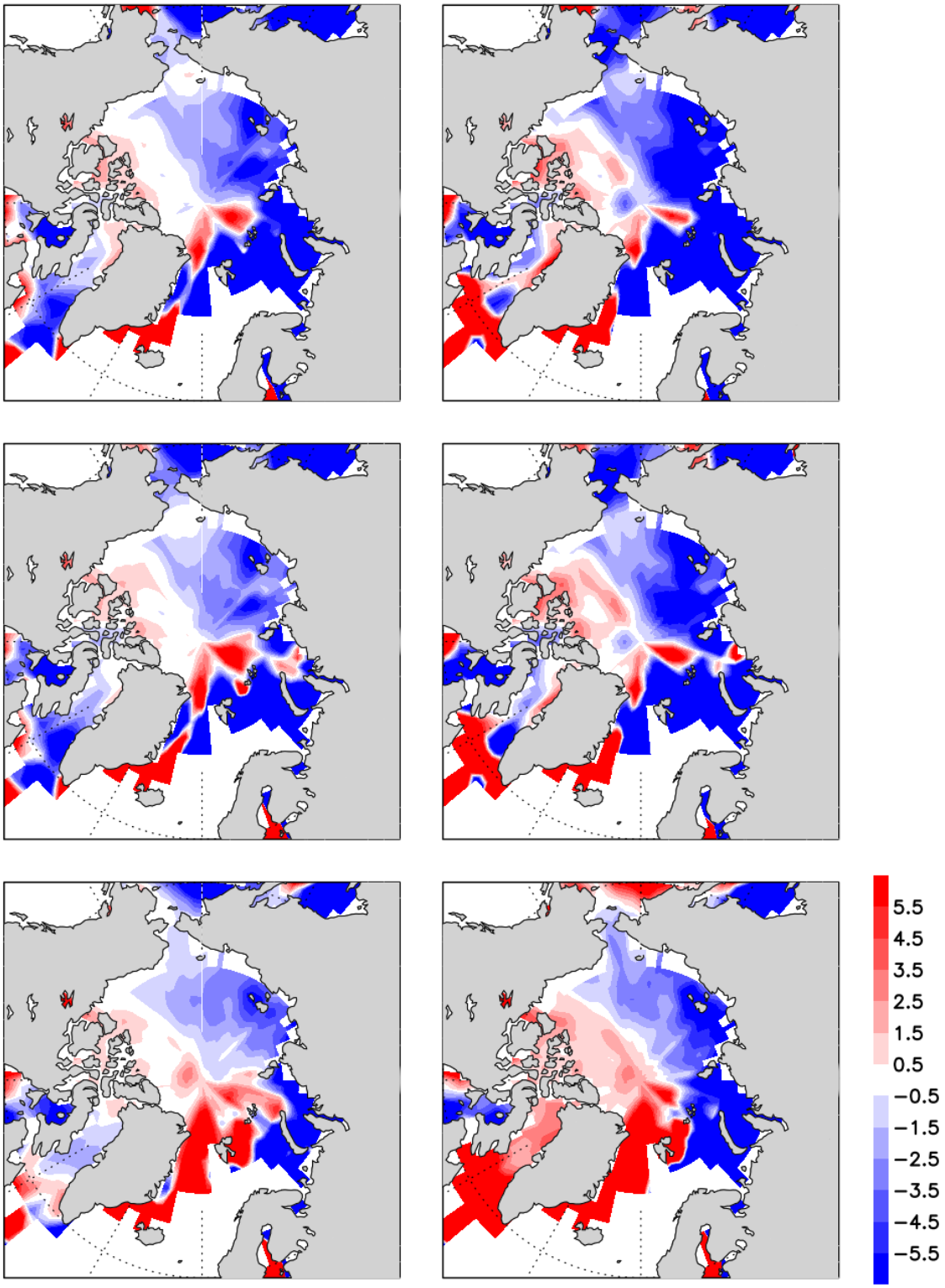

Source: European Commission, JRC, 2016

Figure 14. Trends of BC load related to NAO (10^{-5} mg/m^2/year) as estimated by: NCEP-VA (top left), ERA-VA (top right), NCEP-ST1 (centre left), ERA-ST1 (centre right), NCEP-ST2 (bottom left) and ERA-ST2 (bottom right).

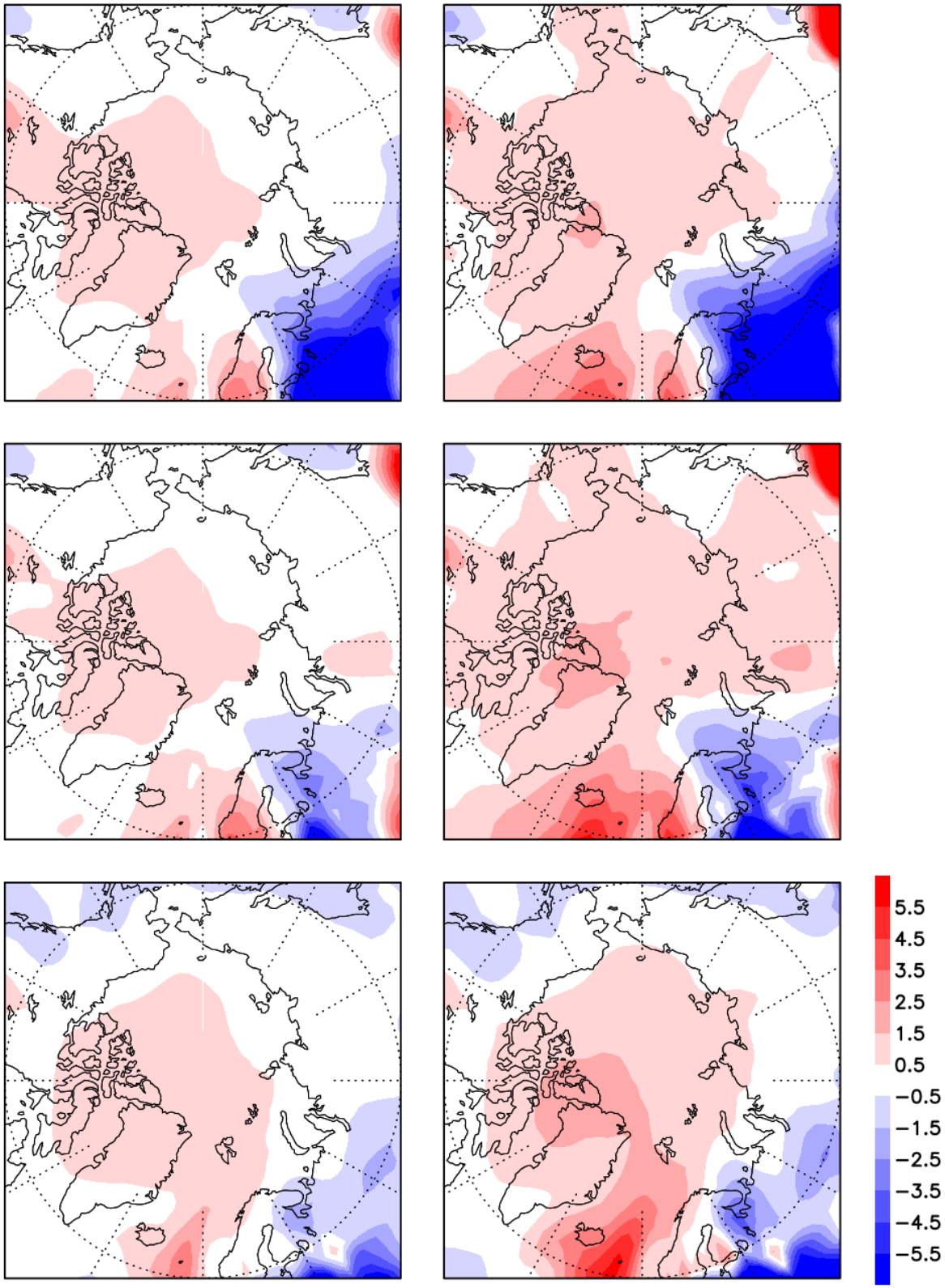

Source: European Commission, JRC, 2016

Figure 15. Trends of BC deposition in February related to NAO ($5*10^{-6}$ ng/m^2/s) as estimated by: NCEP-VA (top left), ERA-VA (top right), NCEP-ST1 (centre left), ERA-ST1 (centre right), NCEP-ST2 (bottom left) and ERA-ST2 (bottom right).

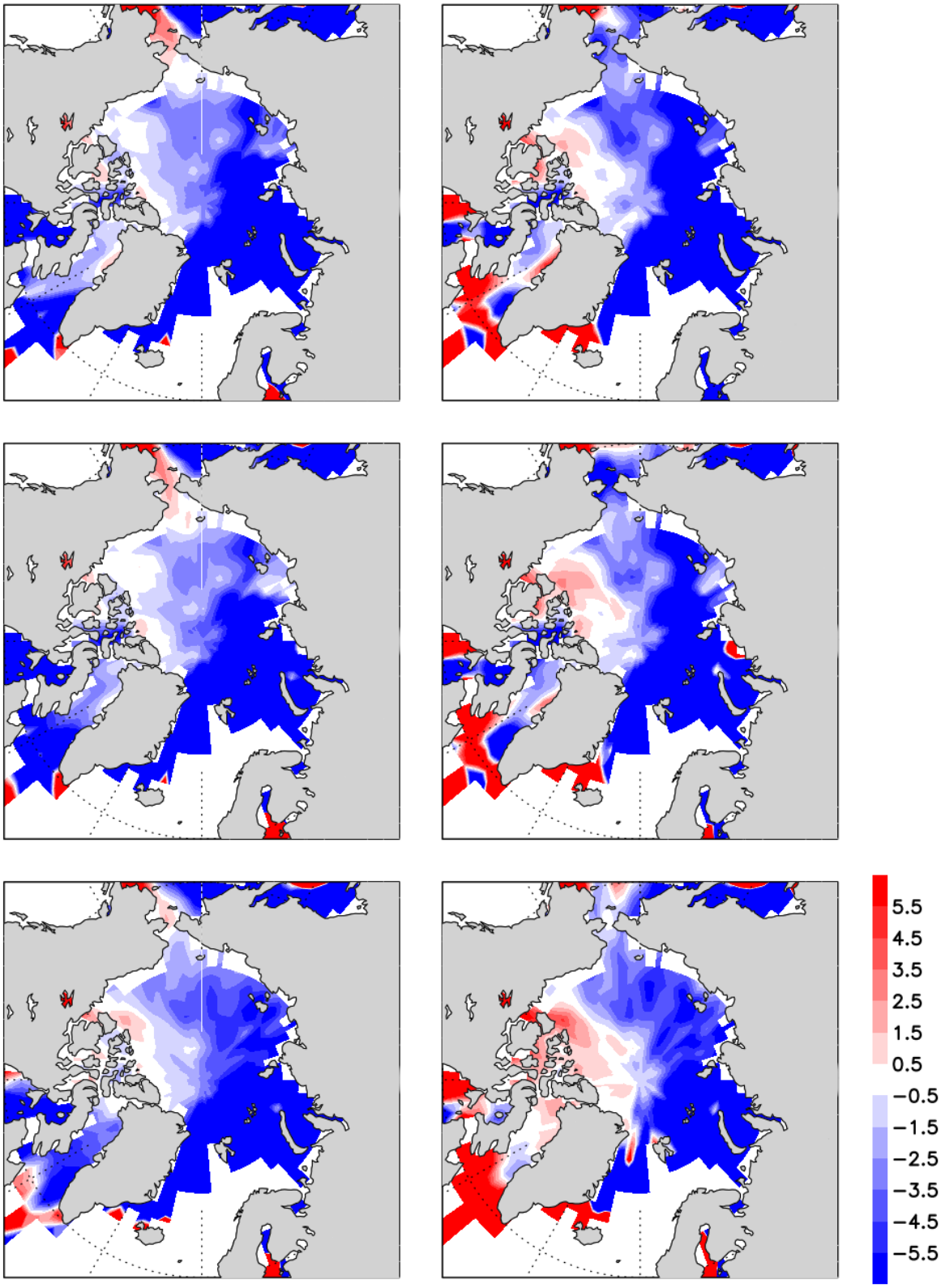

Source: European Commission, JRC, 2016

Figure 16. Trends of BC load in February (10^{-5} mg/m^2/year) related to NAO as estimated by: NCEP-VA (top left), ERA-VA (top right), NCEP-ST1 (centre left), ERA-ST1 (centre right), NCEP-ST2 (bottom left) and ERA-ST2 (bottom right).

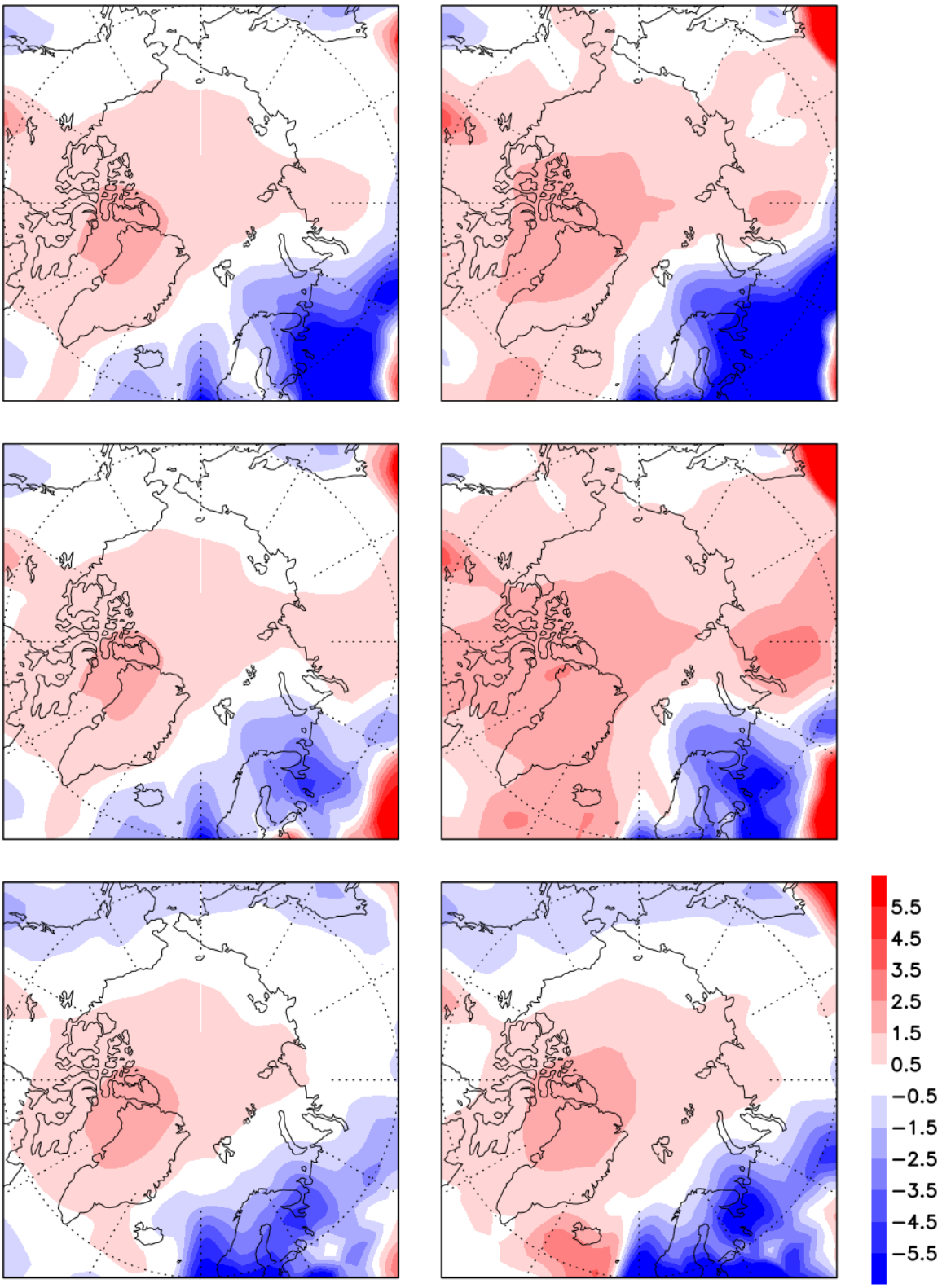

Source: European Commission, JRC, 2016

Figure 17. Trends of BC concentration in February (10^{-3} ng/m^3/year) related to NAO as estimated by NCEP-ST1. Values are averages between 120^{0}W and 30^{0}W and cover the area with the maximum load (see Fig. 4-11). Model level 20 is positioned at 250 mb.

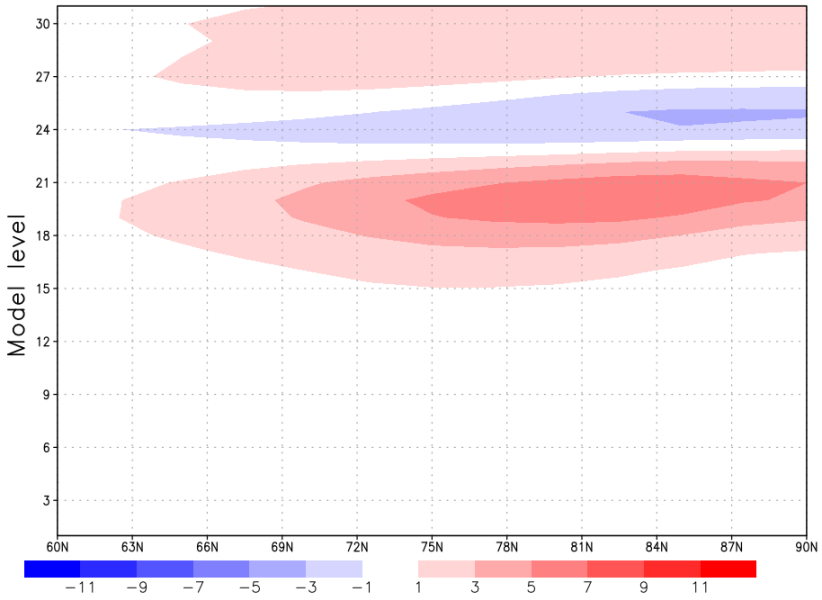

Source: European Commission, JRC, 2016

4.2.2 Black Carbon deposition and load trends related to SB

All estimates of the deposition of BC related to SB show a strong positive trend that extends from the Greenland, Barents and Kara Seas to the central part of the Arctic Ocean (Figure 18). On the other hand, the BC load (Figure 19) does not show any significant trend. The relationship between SB deposition and load trends and the trend of the anticyclonic circulation over Scandinavia is especially evident in February when the Scandinavian anticyclone trend is the most pronounced (Dobricic et al. 2015). Figures 20 and 21 show an even stronger positive deposition trend over most of the Arctic. Only over the Leptev and East Siberian Seas the trend is negative. The positive trend of the load spreads over the Norwegian Sea and Scandinavia indicating the northward advection of the pollution from Europe towards the Arctic Ocean. The vertical structure of the estimated concentration trend (Figure 22) shows that this time the maximum concentration trend is located in the lower troposphere below 3 km and mainly south of the Arctic Ocean. Over the Arctic, however, the concentration trend is very small indicating that the BC advected to the Arctic has been removed from the atmosphere by the wet deposition and deposited on the sea ice.

Figure 18. Trends of BC deposition related to SB ($5*10^{-6}$ ng/m^2/s) as estimated by: NCEP-VA (top left), ERA-VA (top right), NCEP-ST1 (centre left), ERA-ST1 (centre right), NCEP-ST2 (bottom left) and ERA-ST2 (bottom right).

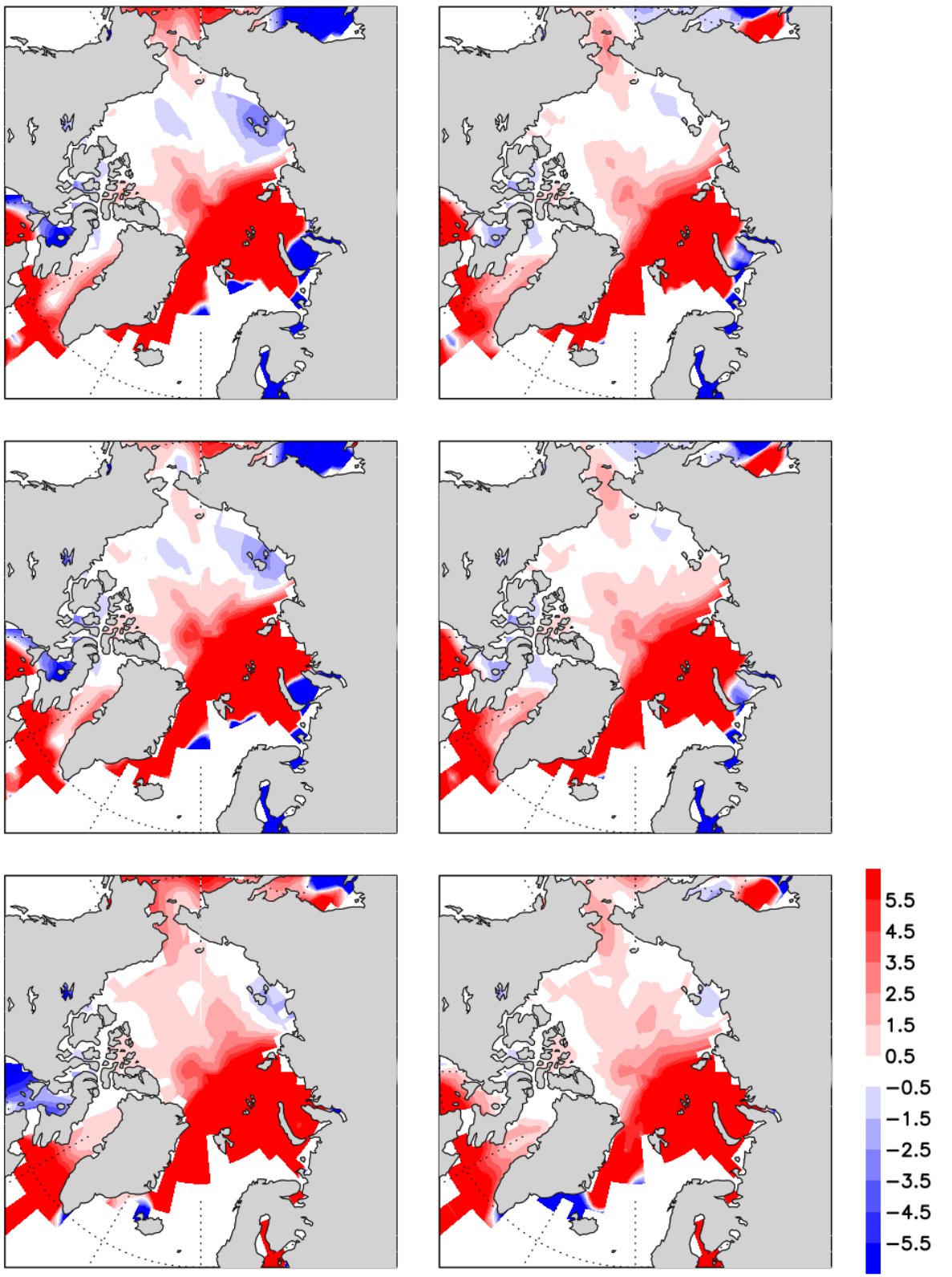

Source: European Commission, JRC, 2016

Figure 19. Trends of BC load (10^{-5} mg/m^2/year) related to SB as estimated by: NCEP-VA (top left), ERA-VA (top right), NCEP-ST1 (centre left), ERA-ST1 (centre right), NCEP-ST2 (bottom left) and ERA-ST2 (bottom right).

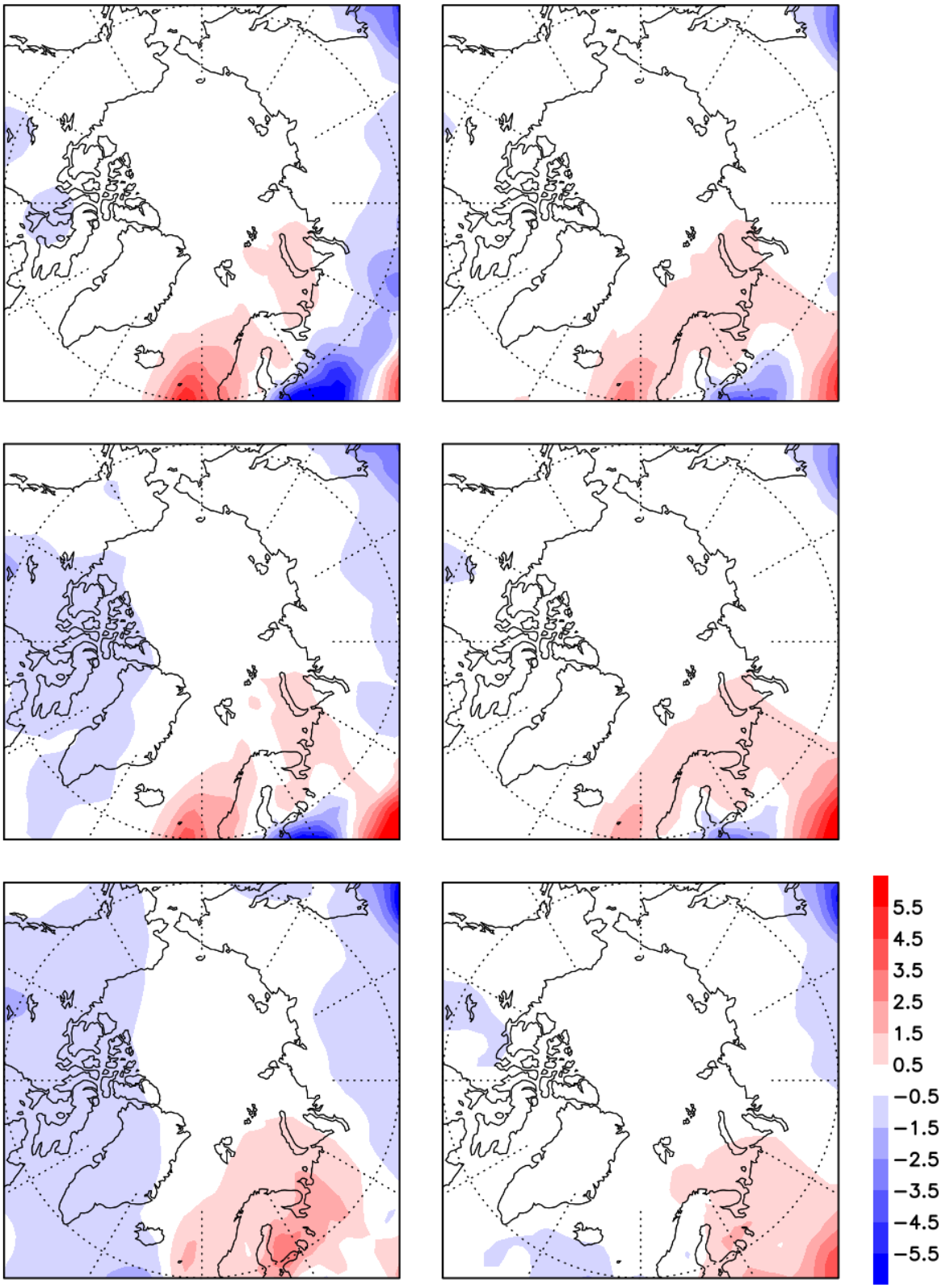

Source: European Commission, JRC, 2016

Figure 20. Trends of BC deposition related to SB in February ($5*10^{-6}$ ng/m^2/s) as estimated by: NCEP-VA (top left), ERA-VA (top right), NCEP-ST1 (centre left), ERA-ST1 (centre right), NCEP-ST2 (bottom left) and ERA-ST2 (bottom right).

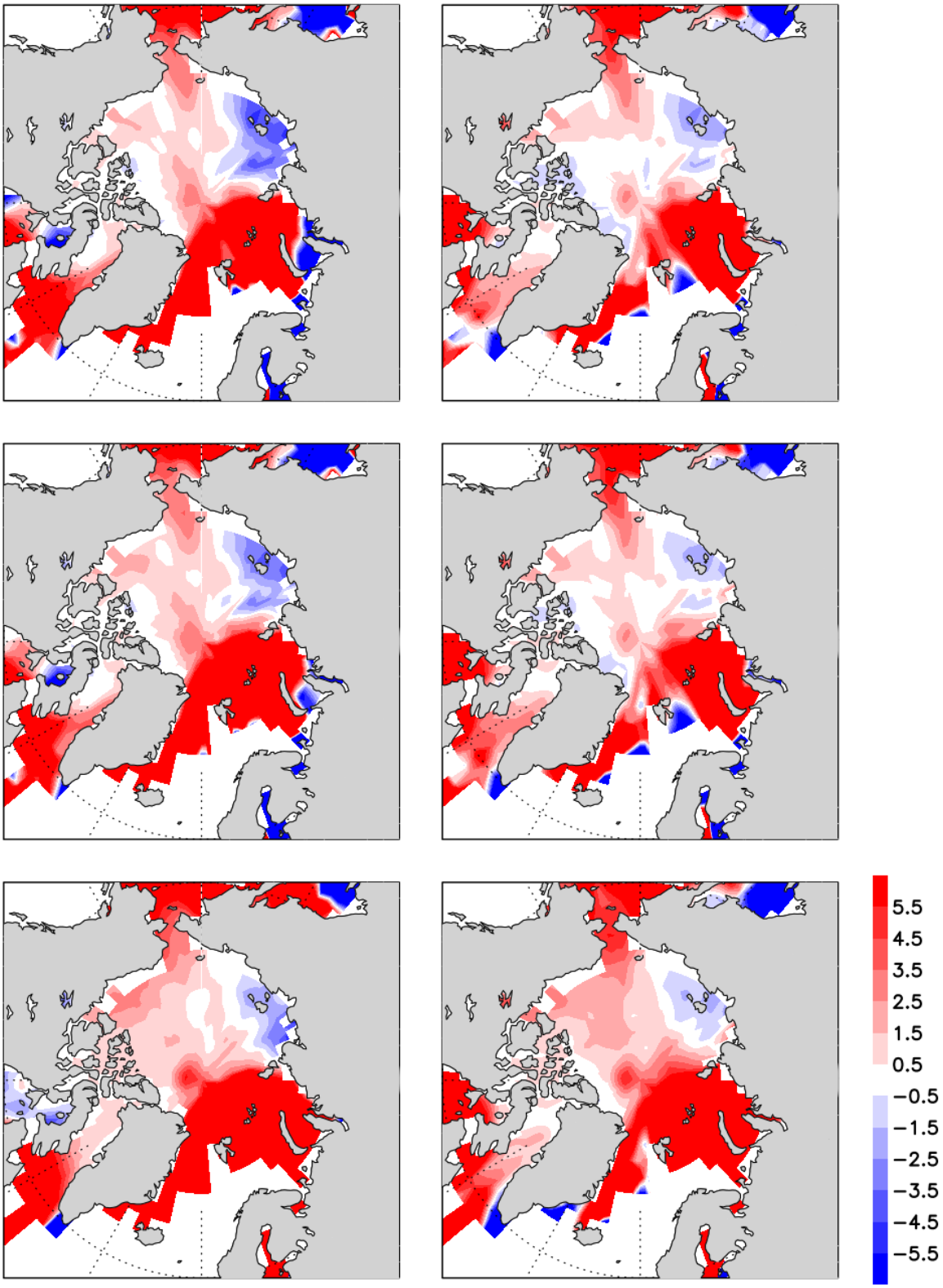

Source: European Commission, JRC, 2016

Figure 21. Trends of BC load (10^{-5} mg/m^2/year) related to SB in February as estimated by: NCEP-VA (top left), ERA-VA (top right), NCEP-ST1 (centre left), ERA-ST1 (centre right), NCEP-ST2 (bottom left) and ERA-ST2 (bottom right).

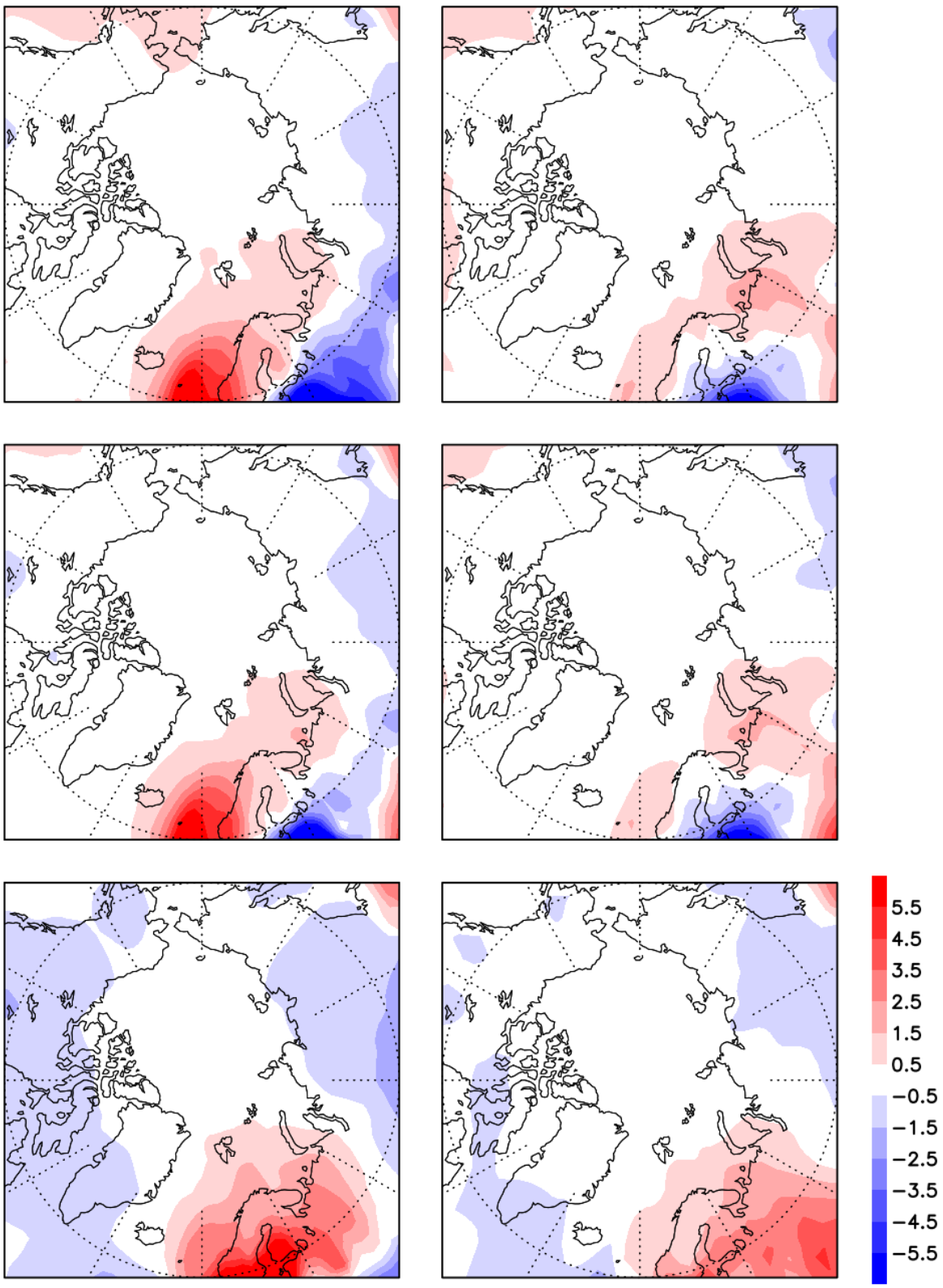

Source: European Commission, JRC, 2016

Figure 22. Trends of BC concentration in February related to SB (10^{-3} ng/m^3/year) as estimated by NCEP-ST1. Values are averages between 30^{0}W and 30^{0}E and cover the area with the maximum load (see Fig. 4-16). Model level 10 is positioned at 700 mb.

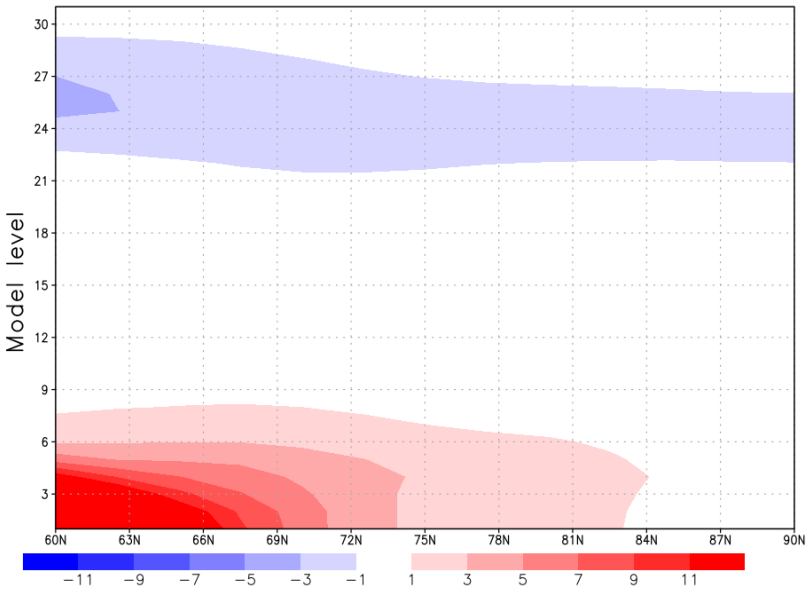

Source: European Commission, JRC, 2016

4.2.3 Black Carbon deposition and load trends related to ENSO

The BC deposition related to ENSO (Figre 23) shows the negative trend over the Barents Sea and a small load tendency over the Arctic (Figure 24). The deposition trend appears to be opposite from the one in SB. This may be due to the cyclonic trend over Scandinavia (Figures 8 and 9). However, the ENSO pattern has a very weak trend in the NCEP reanalysis and its trend is statistically insignificant in the ERA-INTERIM reanalysis. Therefore, we may assume that it is less significant for estimating the impact of the atmospheric transport changes on the BC deposition trend in the Arctic.

Figure 23. Trends of BC deposition related to ENSO ($5*10^{-6}$ ng/m^2/s) as estimated by: NCEP-VA (top left), ERA-VA (top right), NCEP-ST1 (centre left), ERA-ST1 (centre right), NCEP-ST2 (bottom left) and ERA-ST2 (bottom right).

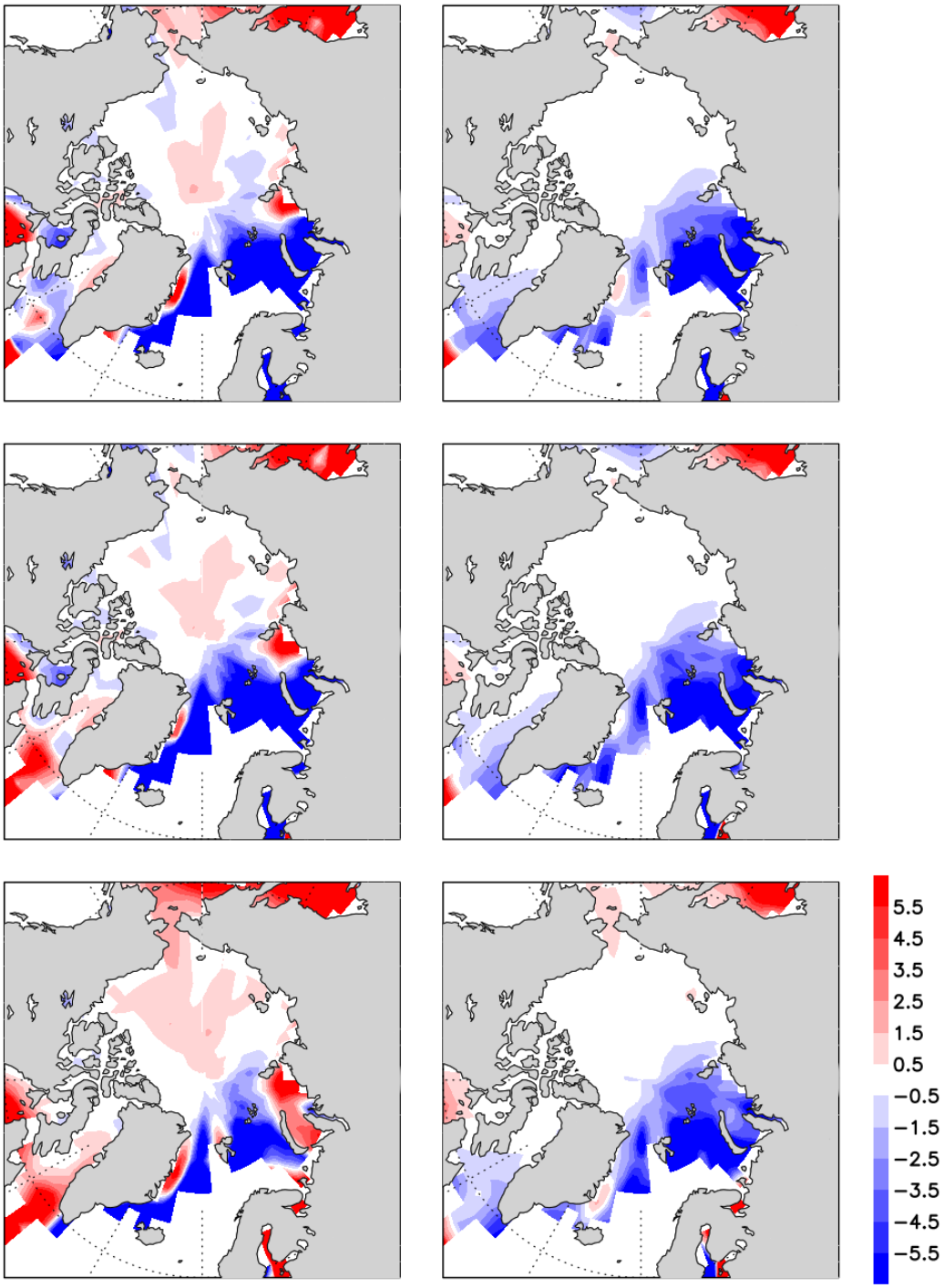

Source: European Commission, JRC, 2016

Figure 24. Trends of BC load (10^{-5} mg/m^2/year) related to ENSO as estimated by: NCEP-VA (top left), ERA-VA (top right), NCEP-ST1 (centre left), ERA-ST1 (centre right), NCEP-ST2 (bottom left) and ERA-ST2 (bottom right).

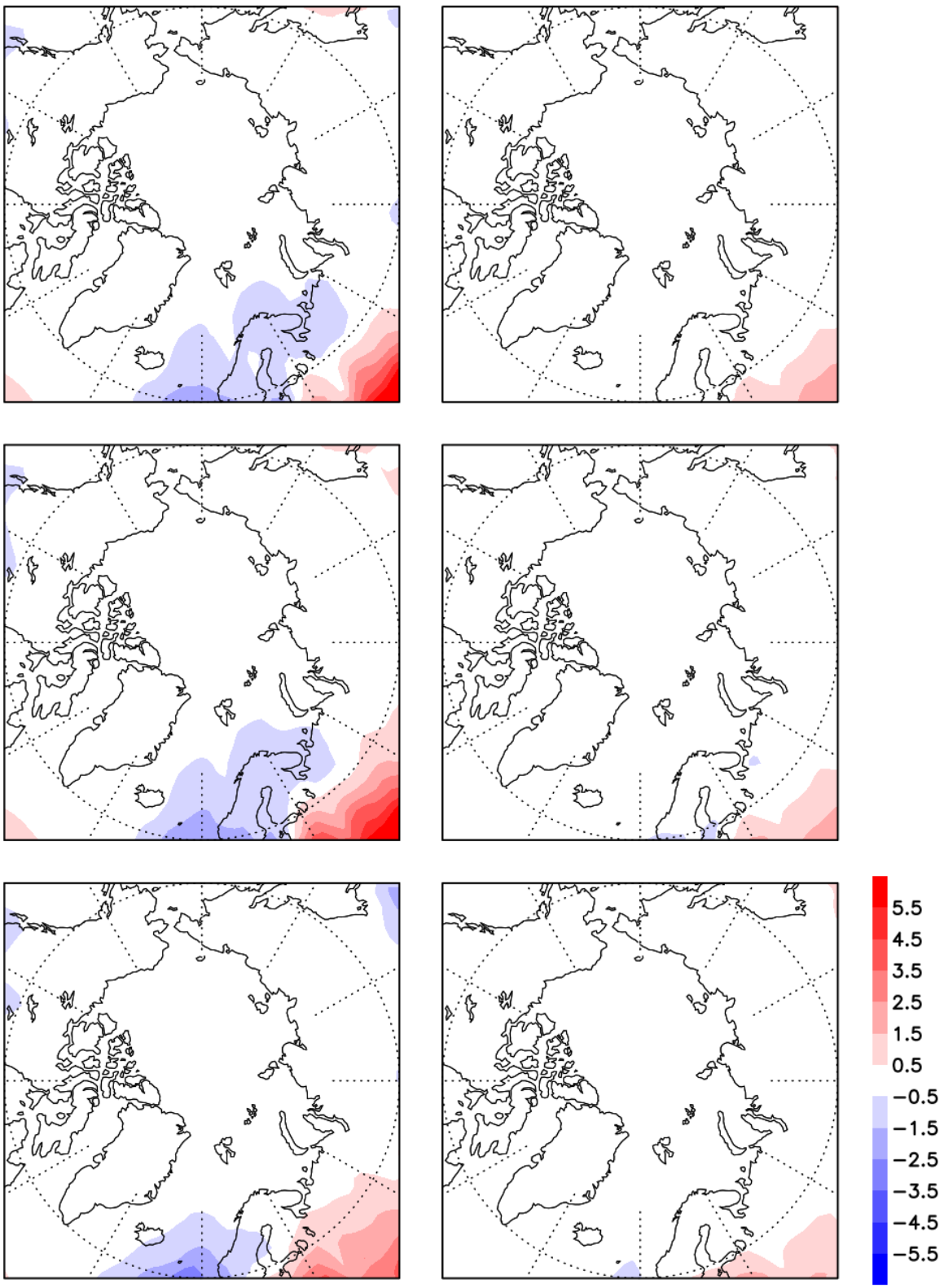

Source: European Commission, JRC, 2016

4.3 Temporal variability of BC deposition

The temporal variability of the BC deposition in the period 1980-2015 may be estimated for any area and for each pattern. In particular it is interesting to evaluate the combined and individual impacts of NAO and SB patterns on the deposition of BC over the Arctic Ocean north of America and Greenland. Figure 25 shows that the NAO pattern produces deposition anomalies with a smaller inter-annual variability than those driven by the SB pattern. Deposition anomalies from the NAO pattern are mostly positive till the year 2000, and after become negative. Those from the SB pattern show a strong increase after the year 2000 that dominates the whole trend from 1980 to 2015. Anomalies estimated from the combination of the two patterns are often very similar to those from the SB pattern, indicating that the SB pattern dominates the variability and the positive trend in this area.

Figure 25. Temporal variability of the BC deposition averaged over the area between 900W-00W and 800N-900N (10^{-4} ng/m^2/s) estimated by NCEP-ST1 and related to: NAO (orange), SB (magenta) and the combined NAO and SB (cyan).

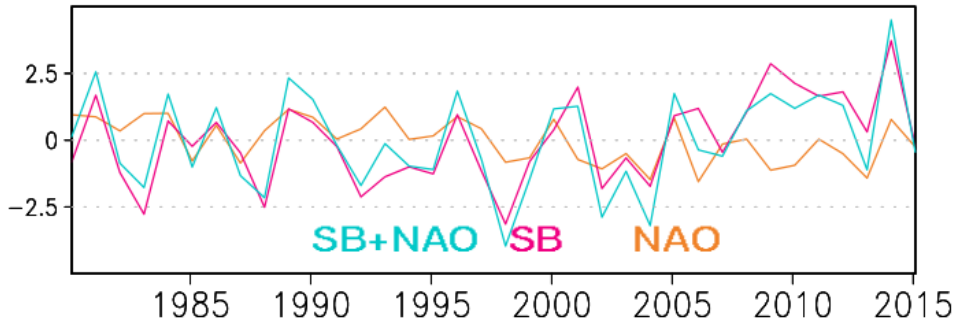

Source: European Commission, JRC, 2016

5 Discussion and conclusions

The study has developed a new statistical algorithm to combine reanalysis estimates of independent components that govern the near-surface warming of the Northern Hemisphere in the winter with model estimates of transport and deposition of black carbon (BC) over the Arctic sea ice. For a given independent component of the atmospheric variability the algorithm estimates the most likelihood deposition and load of BC consistent with the variability of the atmosphere-chemistry coupled model. The algorithm is based on the major assumption that the probabilities of coupled atmosphere-chemistry states are gaussian. The method can be applied without this assumption, but we assume that the gaussianity assumption may alleviate problems that may arise with a small sample size of order of ten by filtering noise from the interesting process. The method is applied with NCEP and ERA-INTERIM atmospheric reanalysis and three realizations of coupled patterns from ECHAM5-HAMMOZ global model simulations.

Previously it has been found that three independent components and their spatial patterns approximate the spatial and temporal structure of the Northern Hemisphere warming trend in the winter (Dobricic et al 2015). They are named according to the prevailing similarity to some well-known atmospheric oscillation patterns as North Atlantic Oscillation (NAO), Scandinavian Blocking (SB) and El-Nino – Southern Oscillation (ENSO). The first two are closely related to the sea ice cover anomaly in the Barents Sea. They, however, differ by the fact that NAO is limited to the mid and high latitudes, while SB connects the temperature anomaly over the Tropical Pacific with temperature and circulation anomalies over the high latitudes. In the period 1980-2015 NAO and SB are associated with the positive trend of the near-surface temperature averaged over the Northern Hemisphere in the winter and with the sea ice melting trend in the Barents Sea.

Although NAO and SB are both linked with the hemispheric temperature increase and the sea ice melting in the Arctic they have significantly different impacts on the BC transport and deposition. NAO mostly reduces the BC deposition with the maximum reduction north of Euro-Asia and the absence of the trend north of America and Greenland. The BC load related to NAO increases over the Arctic. The increase is especially pronounced over the western part of the Arctic Ocean. However, the BC concentration increases inside the anticyclonic anomaly of the circulation with a stable vertical stratification and in the upper troposphere. Therefore, the BC concentration remains suspended high above the ocean and has a small impact on near-surface temperatures and on the deposition of BC. On the other hand, although the BC load over the Arctic related to SB is small compared to the one by NAO, SB directly transports the BC concentration in the lower troposphere from the Northern Atlantic and Europe to the Arctic Ocean. In combination with lower vertical stability the transport in the lower troposphere results in an increasing trend of the BC deposition over a large portion of the Arctic sea ice in the winter. The ENSO pattern has a smaller and statistically less significant impact of the transport and the deposition of BC.

The combined impact of all three atmospheric patterns on deposition trends of BC between 1980 and 2015 (Fig. 4-5) shows that NAO prevails in the eastern part of the Arctic Ocean decreasing the deposition of BC, while in the western and central parts SB prevails and increases the BC deposition. The BC load increases over the whole Arctic. It is mainly governed by the NAO pattern and located in the upper troposphere.

NAO and SB patterns are closely related to the sea ice melting trend in the Arctic Ocean. The statistical analysis has shown that the sea ice melting may often impact the large scale patterns in the high and middle latitudes (Dobricic at al. 2015) and modify the atmospheric transport of pollutants. In this way the sea ice melting may indirectly impact the BC deposition on the sea ice in the winter. The feedback is either negative in some areas of the Arctic Ocean with the decreasing trend of the deposition or positive in other areas with the increasing trend of the deposition. The negative feedback is over the area that in the recent years is characterized by the thin first-year sea ice, while the positive feedback is over the area with the thicker multiyear sea ice (see Fig. 3-1).

During the polar night in the winter the deposited BC has no impact on the sea ice melting. When the sun appears in the spring the short wave radiation starts to melt the fresh snow deposited on the sea ice. The BC impact on the albedo is the most important at the beginning of the melting before the snow melts and becomes darker. Therefore, the BC deposition in the winter may accelerate the initial melting of the snow and by an integrated effect it may result in the increased melting at the end of summer. The first-year sea ice may be completely melted every summer and the decrease of the BC deposition might not be the most important factor controlling its coverage in the late summer. On the other hand, with the increased deposition of BC the multiyear sea ice may melt more and its thickness may become reduced with respect to the previous year. If this process happens consistently over several decades it might significantly contribute to reduction of the thickness of the multiyear sea ice. Our estimate of the temporal variability of the BC

deposition over the multiyear sea ice (Fig. 4-20) indicates that the deposition in the winter due to the sea ice melting feedback increased especially in the last ten years.

In order to further understand the feedback between the global warming process and the trend of the BC deposition it will be necessary to extend the study on other seasons. In particular the major precipitation and wet deposition of BC happen in the summer when also the reduction of the ice cover in the recent years is the largest. Furthermore, although the use of six estimates for atmospheric patterns and coupled atmosphere-chemistry relationships provides some information on the uncertainty of estimates, in the future the method will be applied with several coupled models to further assess the uncertainties.

The increase of the BC deposition due to the sea ice melting feedback emphasizes the importance of the reduction of BC emissions in the mid latitudes. In particular, the SB pattern that is closely related to the global warming transports BC concentrations from the North Atlantic, which frequently originate from emissions in Europe and North America, to the Arctic Ocean and increase the deposition on the multiyear sea ice. Policies that reduce emissions may, therefore, oppose the trend due to the global warming and reduce the risk of the acceleration of the melting of the multiyear sea ice.

References

AMAP, 2011. The Impact of Black Carbon on Arctic Climate (2011). By: P.K. Quinn, A. Stohl, A. Arneth, T. Berntsen, J. F. Burkhart, J. Christensen, M. Flanner, K. Kupiainen, H. Lihavainen, M. Shepherd, V. Shevchenko, H. Skov, and V. Vestreng. Arctic Monitoring and Assessment Programme (AMAP), Oslo. 72 pp.

AMAP Assessment 2015: Black carbon and ozone as Arctic climate forcers. Arctic Monitoring and Assessment Programme (AMAP), Oslo, Norway. vii + 116 pp.

Aoki, T. et al. Effects of snow physical parameters on spectral albedo and bidirectional reflectance of snow surface. J. Geophys. Res. 105, 10219-10236 (2000).

Auvray, M., Bey, I., Llull, E., Schultz, M. G., and Rast, S.: A model investigation of tropospheric ozone chemical tendencies in long-range transported pollution plumes, J. Geophys. Res., 112, D05304, doi:10.1029/2006JD007137, 2007.

Browse, J., K.S. Carslaw, S. Arnold, K.J. Pringle and O. Boucher, 2012. The scavenging processes controlling the seasonal cycle in Arctic sulphate and black carbon aerosol. Atmospheric Chemistry and Physics, 12:6775-6798.

Bourgeois, Q. and I. Bey, 2011. Pollution transport efficiency toward the Arctic: Sensitivity to aerosol scavenging and source regions. Journal of Geophysical Research: Atmospheres, 116:D08213, doi:10.1029/2010JD015096.

Byrd, R.H., Lu, P., Nocedal, J., Zhu, C., 1995. A limited memory algorithm for bound constrained optimization. SIAM Journal on Scientific Computing 16, 1190–1208.

Cohen, J., J., A. Screen, J. C. Furtado, M. Barlow, D. Whittleston, D. Coumou, J. Francis, K. Dethloff, D. Entekhabi, J. Overland, and J. Jones, 2014: Recent Arctic amplification and extreme mid-latitude weather. Nature Geosci., 7, 627–637.

Comiso, J. C. (2012), Large decadal decline of the Arctic multiyear ice cover, J. Clim., 25, 1176–1193, doi:10.1175/JCLI-D-11-00113.1.

Conway, H., A. Gades and C.F. Raymond, 1996. Albedo of dirty snow during conditions of melt. Water Resources Research, 32:1713-1718.

Dee, D.P., S.M. Uppala, S. M., A. J. Simmons, P. Berrisford, P. Poli, S. Kobayashi, S. U. Andrae, M. A. Balmaseda, G. Balsamo, P. Bauer, P. Bechtold, A. C. M. Beljaars, L. van de Berg, J. Bidlot, N. Bormann, C. Delsol, R. Dragani, M. Fuentes, A. J. Geer, L. Haimberger, S. B. Healy, H. Hersbach, E. V. Holm, L. Isaksen, P. Kallberg, M. Kohler, M. Matricardi, A. P. Mcnally, B. M. Monge-Sanz, J.-J. Morcrette, B.-K. Park, C. Peubey, P. de Rosnay, C. Tavolato, J.-N. Thepaut, F. Vitart, 2011: The ERA-Interim reanalysis: Configuration and performance of the data assimilation system. Q. J. Roy. Met. Soc., 137, 553–597.

Deser, C., R. A. Tomas, and S. Peng, 2007: The transient atmospheric circulation response to North Atlantic SST and sea ice anomalies. J. Clim., 20, 4751–4767.

Diehl, T., Heil, A., Chin, M., Pan, X., Streets, D., Schultz, M., and Kinne, S.: Anthropogenic, biomass burning, and volcanic emissions of black carbon, organic carbon, and SO2 from 1980 to 2010 for hindcast model experiments, Atmos. Chem. Phys. Discuss., 12, 24895-24954, doi:10.5194/acpd-12-24895-2012, 2012.

Dobricic, S., Vignati, E., and S. Russo S, 2015, Large scale atmospheric warming in the winter and the Arctic sea ice retreat, submitted to J. Clim.

Doherty, S.J., S.G. Warren, T.C. Grenfell, A.D. Clarke and R.E. Brandt, 2010. Light-absorbing impurities in Arctic snow. Atmospheric Chemistry and Physics, 10:11647-11680.

Döscher, R., Vihma, T., and Maksimovich, E.: Recent advances in understanding the Arctic climate system state and change from a sea ice perspective: a review, Atmos. Chem. Phys., 14, 13571-13600, doi:10.5194/acp-14-13571-2014, 2014.

Eckhardt, S., Quennehen, B., Olivié, D. J. L., Berntsen, T. K., Cherian, R., Christensen, J. H., Collins, W., Crepinsek, S., Daskalakis, N., Flanner, M., Herber, A., Heyes, C., Hodnebrog, Ø., Huang, L., Kanakidou, M., Klimont, Z., Langner, J., Law, K. S., Lund, M. T., Mahmood, R., Massling, A., Myriokefalitakis, S., Nielsen, I. E., Nøjgaard, J. K., Quaas, J., Quinn, P. K., Raut, J.-C., Rumbold, S. T., Schulz, M., Sharma, S., Skeie, R. B., Skov, H., Uttal, T., von Salzen, K., and Stohl, A.: Current model capabilities for simulating black carbon and sulfate concentrations in

the Arctic atmosphere: a multi-model evaluation using a comprehensive measurement data set, Atmos. Chem. Phys., 15, 9413-9433, doi:10.5194/acp-15-9413-2015, 2015.

Endresen, A., Sorgard, E., Sundet, J. K., Dalsoren, S. B., Isaksen, I. S. A., Berglen, T. F., and Gravir, G.: Emission from international sea transportation and environmental impact, J. Geophys. Res., 108, 4560, doi:10.1029/2002JD002898, 2003.

Eyring, V., Isaksen I. S. A., Berntsen, T., Collins, W. J., Corbett, J. J., Endresen, O., Grainger, R. G., Moldanova, J., Schlager, H., and Stevenson, D. S.: Transport impacts on atmosphere and climate: Shipping, Atmos. Environ., 44, 4735–4771, doi:10.1016/j.atmosenv.2009.04.059, 2010.

Flanner, M. G. & Zender, C. S. Linking snowpack microphysics and albedo evolution. J. Geophys. Res. 111, D12208 (2006).

Flanner, M. G. Arctic climate sensitivity to local black carbon. J. Geophys. Res. Atmos. 118, 18401851 (2013).

Gascard, J. C., Festy, J., le Goff, H., Weber, M., Bruemmer, B., Offermann, M., and Bottenheim, J.: Exploring Arctic transpolar drift during dramatic sea ice retreat, EOS T. Am. Geophys. Un., 89, 21–22, 2008.

Hadley, O. L. and Kirchstetter, T. W.: Black-carbon reduction of snow albedo, Nature Climate Change, 2, 437–440, doi:10.1038/nclimate143310.1038/NCLIMATE1433, 2012.

Häkkinen, S., Proshutinsky, A., and Ashik, I.: Sea ice drift in the Arctic since the 1950s, Geophys. Res. Lett., 35, L19704, doi:10.1029/2008GL034791, 2008.

Hannachi, A., S. Unkel, N. T. Trendafilov, and I. T. Jolliffe, 2009: Independent Component Analysis of Climate Data: A New Look at EOF Rotation. J. Clim., 22, 2797–2812.

Hirdman, D., J.F. Burkhart, H. Sodemann, S. Eckhardt, A. Jefferson, P.K. Quinn, S. Sharma, J. Ström and A. Stohl, 2010a. Long-term trends of black carbon and sulphate aerosol in the Arctic: changes in atmospheric transport and source region emissions. Atmospheric Chemistry and Physics, 10:9351-9368.

Hyvärinen, A., and E. Oja, 2000: Independent component analysis: algorithms and applications. Neural networks, 13, 411–430.

Hyvärinen, A., 2012: Independent component analysis: recent advances. Phil. Trans. R. Soc. A, 371 20110534, doi:10.1098/rsta.2011.0534.

Jennrich, R. I., and N. T. Trendafilov, 2005: Independent component analysis as a rotation method: A very different solution to Thurstone's box problem. Br. J. Math. Stat. Psychol., 58, 199–208.

Jiao, C., M.G. Flanner, Y. Balkanski, S.E. Bauer, N. Bellouin, T.K. Berntsen, H. Bian, K.S. Carslaw, M. Chin, N. De Luca, T. Diehl, S.J. Ghan, T. Iversen, A. Kirkevåg, D. Koch, X. Liu, G.W. Mann, J.E. Penner, G. Pitari, M. Schulz, Ø. Seland, R.B. Skeie, S.D. Steenrod, P. Stier, T. Takemura, K. Tsigaridis, T. van Noije, Y. Yun and K. Zhang, 2014. An AeroCom assessment of black carbon in Arctic snow and sea ice. Atmospheric Chemistry and Physics, 14:2399-2417.

Kalnay, E., M. Kanamitsu, R. Kistler, W. Collins, D. Deaven, L. Gandin, M. Iredell, S. Saha, G. White, J. Woollen, Y. Zhu, A. Leetmaa, R. Reynolds, M. Chelliah, W. Ebisuzaki, W. Higgins, J. Janowiak, K. C. Mo, C. Ropelewski, J. Wang, Roy Jenne, and Dennis Joseph, 1996: The NCEP/NCAR 40-year reanalysis project. Bull. Am. Meteorol. Soc., 77, 437–470.

Kim, D., Chin, M., Yu, H., Diehl, T., Tan, Q., Kahn, R.A., Tsigaridis, K., Bauer, S.E., Takemura, T., Pozzoli, L., Bellouin, N., Schulz, M., Peyridieu, S., Chédin, A., Koffi, B.: Sources, sinks, and transatlantic transport of North African dust aerosol: A multimodel analysis and comparison with remote sensing data, (2014) Journal of Geophysical Research: Atmospheres, 119 (10), pp. 6259-6277. doi:10.1002/2013JD021099

Kinnison, D. E., Brasseur, G. P., Walters, S., Gracia, R. R., Marsh, D. R., Sassi, F., Harvey, V. L., Randall, C. E., Emmons, L., Lamarque, J. F., Hess, P., Orlando, J. J., Tie, X. X., Randel, W., Pan, L. L., Gettelman, A., Granier, C., Diehl, T., Niemeier, U., and Simmons, A. J.: Sensitivity of chemical tracers to meteorological parameters in the MOZART- 3 chemical transport model, J. Geophys. Res, 112, D20302, doi:10.1029/2006JD007879, 2007.

Kwok, R.: Outflow of Arctic Ocean sea ice into the Greenland and Barents Seas: 1979–2007, J. Climate, 22, 2438–2457, 2009.

Kwok, R. and Rothrock, D. A.: Decline in Arctic sea ice thickness from submarine and ICESat records: 1958–2008, Geophys. Res. Lett., 36, L15501, doi:10.1029/2009GL039035, 2009.

Liu, J., S. Fan, L. Horowitz and H. Levy, 2011. Evaluation of factors controlling long-range transport of black carbon to the Arctic. Journal of Geophysical Research: Atmospheres, 116:D04307, doi:10.1029/2010JD015145.

Mann, H. B., 1945: Non-parametric tests against trend, Econometrica, 13, 163-171.

Maslanik, J., Stroeve, J., Fowler, C., and Emery, W.: Distribution and trends in Arctic sea ice age through spring 2011, Geophys. Res. Lett., 38, L13502, doi:10.1029/2011GL047735, 2011.

Mori, M., M. Watanabe, H. Shiogama, J. Inoue, and M. Kimoto, 2014: Robust Arctic sea-ice influence on the frequent Eurasian cold winters in past decades. Nature Geosci., 7, 869–873.

Overland, J. E., and M. Wang, 2010: Large-scale atmospheric circulation changes are associated with the recent loss of Arctic sea ice. Tellus A, 62, 1-9.

Pan, X., Chin, M., Gautam, R., Bian, H., Kim, D., Colarco, P.R., Diehl, T.L., Takemura, T., Pozzoli, L., Tsigaridis, K., Bauer, S., Bellouin, N.: A multi-model evaluation of aerosols over South Asia: Common problems and possible causes, (2015) Atmospheric Chemistry and Physics, 15 (10), pp. 5903-5928. doi:10.5194/acp-15-5903-2015

Pausata, F.S.R., Pozzoli, L., Dingenen, R.V., Vignati, E., Cavalli, F., Dentener, F.J.: Impacts of changes in North Atlantic atmospheric circulation on particulate matter and human health in Europe, (2013) Geophysical Research Letters, 40 (15), pp. 4074-4080. doi:10.1002/grl.50720

Pausata, F.S.R., Pozzoli, L., Vignati, E., Dentener, F.J.: North Atlantic Oscillation and tropospheric ozone variability in Europe: Model analysis and measurements intercomparison, (2012) Atmospheric Chemistry and Physics, 12 (14), pp. 6357-6376. doi:10.5194/acp-12-6357-2012

Petoukhov, V., and V. A. Semenov, 2010: A link between reduced Barents-Kara sea ice and cold winter extremes over northern continents. J. Geophys. Res., 115, D21111.

Pozzoli, L., Janssens-Maenhout, G., Diehl, T., Bey, I., Schultz, M. G., Feichter, J., Vignati, E., and Dentener, F.: Re-analysis of tropospheric sulfate aerosol and ozone for the period 1980–2005 using the aerosol-chemistry-climate model ECHAM5-HAMMOZ, Atmos. Chem. Phys., 11, 9563-9594, doi:10.5194/acp-11-9563-2011, 2011.

Pozzoli, L., Bey, I., Rast, S., Schultz, M. G., Stier, P., and Feichter, J.: Trace gas and aerosol interactions in the fully coupled model of aerosol-chemistry-climate ECHAM5- HAMMOZ: 1. Model description and insights from the spring 2001 TRACE-P experiment, J. Geophys. Res., 113, D07308, doi:10.1029/2007JD009007, 2008a.

Pozzoli, L., Bey, I., Rast, S., Schultz, M. G., Stier, P., and Feichter, J.: Trace gas and aerosol interactions in the fully coupled model of aerosol-chemistry-climate ECHAM5-HAMMOZ: 2. Impact of heterogeneous chemistry on the global aerosol distributions, J. Geophys. Res., 113, D07309, doi:10.1029/2007JD009008, 2008b.

Rast, S., MG. Schultz, I. Bey, T. van Noije, co-authors. Evaluation of the tropospheric chemistry general circulation model ECHAM5–MOZ and its application to the analysis of the chemical composition of the troposphere with an emphasis on the late RETRO period 1990–2000. Technisch rapport: 2014, Max Planck Institute of Meteorology, Earth System Science, 74p. (Available at http://www.mpimet.mpg.de/fileadmin/publikationen/Reports/WEB_BzE_114.pdf)

Rothrock, D. A., Percival, D. B., and Wensnahan, M.: The decline in arctic sea-ice thickness: separating the spatial, annual, and interannual variability in a quarter century of submarine data, J. Geophys. Res., 113, C05003, doi:10.1029/2007JC004252, 2008.

Sand, M., T. Berntsen, J.E. Kay, J.F. Lamarque, Ø. Seland and A. Kirkevåg, 2013a. The arctic response to remote and local forcing of black carbon. Atmospheric Chemistry and Physics, 13:211-224.

Sand, M., T. Berntsen, Ø. Seland and J.E. Kristjánsson, 2013b. Arctic surface temperature change to emissions of black carbon within Arctic or midlatitudes. Journal of Geophysical Research: Atmospheres, 118:7788-7798.

Schultz, M., Backman, L., Balkanski, Y., Bjoerndalsaeter, S., Brand, R., Burrows, J., Dalsoeren, S., de Vasconcelos, M., Grodtmann, B., Hauglustaine, D., Heil, A., Hoelzemann, J., Isaksen, I., Kaurola, J., Knorr, W., Ladstaetter-Weienmayer, A., Mota, B., Oom, D., Pacyna, J., Panasiuk, D., Pereira, J., Pulles, T., Pyle, J., Rast, S., Richter, A., Savage, N., Schnadt, C., Schulz, M., Spessa, A., Staehelin, J., Sundet, J., Szopa, S., Thonicke, K., van het Bolscher, M., van Noije, T., van Velthoven, P., Vik, A., and Wittrock, F.: REanalysis of the TROpospheric chemical composition over the past 40 years (RETRO). A long-term global modeling study of tropospheric chemistry. Final Report, Tech. rep., Max Planck Institute for Meteorology, Hamburg, Germany, 2007.

Schultz, M. G., Heil, A., Hoelzemann, J. J., Spessa, A., Thonicke, K., Goldammer, J. G., Held, A. C., Pereira, J. M. C., and van het Bolscher, M.: Global wildland fire emissions from 1960 to 2000, Global Biogeochem. Cy., 22, GB2002, doi:10.1029/2007GB003031, 2008.

Screen, J. A., Simmonds, I., and Keay, K.: Dramatic interannual changes of perennial Arctic sea ice linked to abnormal summer storm activity, J. Geophys. Res., 116, D15105, doi:10.1029/2011JD015847, 2011.

Screen, J., I. Simmonds, C. Deser, and R. Tomas, 2013: The atmospheric response to three decades of observed Arctic Sea ice loss. J. Clim., 26, 1230–1248. doi:10.1175/JCLI-D-12-00063.1

Semenov, V. A., and Latif, M..: Nonlinear winter atmospheric circulation response to Arctic sea ice concentration anomalies for different periods during 1966–2012. Environmental Research Letters 10, 2015.

Sen, P.K., 1968: Estimates of the regression coefficient based on Kendall's tau. J. Am. Stat. Assoc., 63, 1379–1389.

Shindell, D. T. and Faluvegi, G. Climate response to regional radiative forcing during the twentieth century. Nature Geosci. 2, 294-300 (2009).

Smedsrud, L. H., et al. (2013), The role of the Barents Sea in the Arctic climate system, Rev. Geophys., 51, 415–449, doi:10.1002/rog.20017.

Stier, P., Feichter, J., Kinne, S., Kloster, S., Vignati, E., Wilson, J., Ganzeveld, L., Tegen, I., Werner, M., Balkanski, Y., Schulz, M., Boucher, O., Minikin, A., and Petzold, A.: The aerosolclimate model ECHAM5-HAM, Atmos. Chem. Phys., 5, 1125– 1156, doi:10.5194/acp-5-1125-2005, 2005.

Stohl, A., 2006. Characteristics of atmospheric transport into the Arctic troposphere. Journal of Geophysical Research: Atmospheres, 111:D11306, doi:10.1029/2005JD006888.

Tsigaridis, K., Daskalakis, N., Kanakidou, M., Adams, P.J., Artaxo, P., Bahadur, R., Balkanski, Y., Bauer, S.E., Bellouin, N., Benedetti, A., Bergman, T., Berntsen, T.K., Beukes, J.P., Bian, H., Carslaw, K.S., Chin, M., Curci, G., Diehl, T., Easter, R.C., Ghan, S.J., Gong, S.L., Hodzic, A., Hoyle, C.R., Iversen, T., Jathar, S., Jimenez, J.L., Kaiser, J.W., Kirkeväg, A., Koch, D., Kokkola, H., H Lee, Y., Lin, G., Liu, X., Luo, G., Ma, X., Mann, G.W., Mihalopoulos, N., Morcrette, J.-J., Müller, J.-F., Myhre, G., Myriokefalitakis, S., Ng, N.L., O'donnell, D., Penner, J.E., Pozzoli, L., Pringle, K.J., Russell, L.M., Schulz, M., Sciare, J., Seland, Ø., Shindell, D.T., Sillman, S., Skeie, R.B., Spracklen, D., Stavrakou, T., Steenrod, S.D., Takemura, T., Tiitta, P., Tilmes, S., Tost, H., Van Noije, T., Van Zyl, P.G., Von Salzen, K., Yu, F., Wang, Z., Wang, Z., Zaveri, R.A., Zhang, H., Zhang, K., Zhang, Q., Zhang, X.: The AeroCom evaluation and intercomparison of organic aerosol in global models, (2014) Atmospheric Chemistry and Physics, 14 (19), pp. 10845-10895. doi:10.5194/acp-14-10845-2014

Yasunari, T. J., Koster, R. D., Lau, K. M., Aoki, T., Sud, Y. C., Yamazaki, T., Motoyoshi, H., and Kodama, Y.: Influence of dust and black carbon on the snow albedo in the NASA Goddard Earth Observing System version 5 land surface model, J. Geophys. Res., 116, D02210, doi:10.1029/2010JD014861, 2011.

Uppala, S. M., KAllberg, P. W., Simmons, A. J., Andrae, U., Bech- ˚ told, V. D. C., Fiorino, M., Gibson, J. K., Haseler, J., Hernandez, A., Kelly, G. A., Li, X., Onogi, K., Saarinen, S., Sokka, N., Allan, R. P., Andersson, E., Arpe, K., Balmaseda, M. A., Beljaars, A. C. M., Berg, L. V. D., Bidlot, J., Bormann, N., Caires, S., Chevallier, F., Dethof, A., Dragosavac, M., Fisher, M., Fuentes, M., Hagemann, S., Holm, E., Hoskins, B. J., Isaksen, L., Janssen, ´ P. A. E. M., Jenne, R., Mcnally, A. P., Mahfouf, J.-F., Morcrette, J.-J., Rayner, N. A., Saunders, R. W., Simon, P., Sterl, A., Trenberth, K. E., Untch, A., Vasiljevic, D., Viterbo, P., and Woollen, J.: The ERA-40 re-analysis, Q. J. Roy. Meteorol. Soc., 131, 2961–3012, doi:10.1256/qj.04.176, 2005.

van der Werf, G. R., Randerson, J. T., Giglio, L., Collatz, G. J., Mu, M., Kasibhatla, P. S., Morton, D. C., DeFries, R. S., Jin, Y., and van Leeuwen, T. T.: Global fire emissions and the contribution of deforestation, savanna, forest, agricultural, and peat fires (1997–2009), Atmos. Chem. Phys., 10, 11707–11735, doi:10.5194/acp-10-11707-2010, 2010.

List of abbreviations and definitions

AMAP	Arctic Monitoring and Assessment Programme
BC	Black Carbon
ECMWF	European Centre for Medium-Range Weather Forecasts
ENSO	El Nino – Southern Oscillation
EOF	Empirical Orthogonal Function
ICA	Independent Component Analysis
NAO	North Atlantic Oscillation
NCEP	National Center for Environmental Prediction
SB	Scandinavian Blocking

List of figures

List of tables

GETTING IN TOUCH WITH THE EU

In person

All over the European Union there are hundreds of Europe Direct information centres. You can find the address of the centre nearest you at: https://europa.eu/european-union/contact_en

On the phone or by email

Europe Direct is a service that answers your questions about the European Union. You can contact this service:

- by freephone: 00 800 6 7 8 9 10 11 (certain operators may charge for these calls),

- at the following standard number: +32 22999696, or

- by electronic mail via: https://europa.eu/european-union/contact_en

FINDING INFORMATION ABOUT THE EU

Online

Information about the European Union in all the official languages of the EU is available on the Europa website at: https://europa.eu/european-union/index_en

EU publications

You can download or order free and priced EU publications from EU Bookshop at: https://publications.europa.eu/en/publications. Multiple copies of free publications may be obtained by contacting Europe Direct or your local information centre (see https://europa.eu/european-union/contact_en).

LB-NA-27711-EN-N

The European Commission's science and knowledge service

Joint Research Centre

JRC Mission

As the science and knowledge service of the European Commission, the Joint Research Centre's mission is to support EU policies with independent evidence throughout the whole policy cycle.

EU Science Hub

ec.europa.eu/jrc

@EU_ScienceHub

EU Science Hub - Joint Research Centre

EU Science, Research and Innovation

EU Science Hub

Publications Office of the European Union

doi:10.2788/879160

ISBN 978-92-79-54639-6